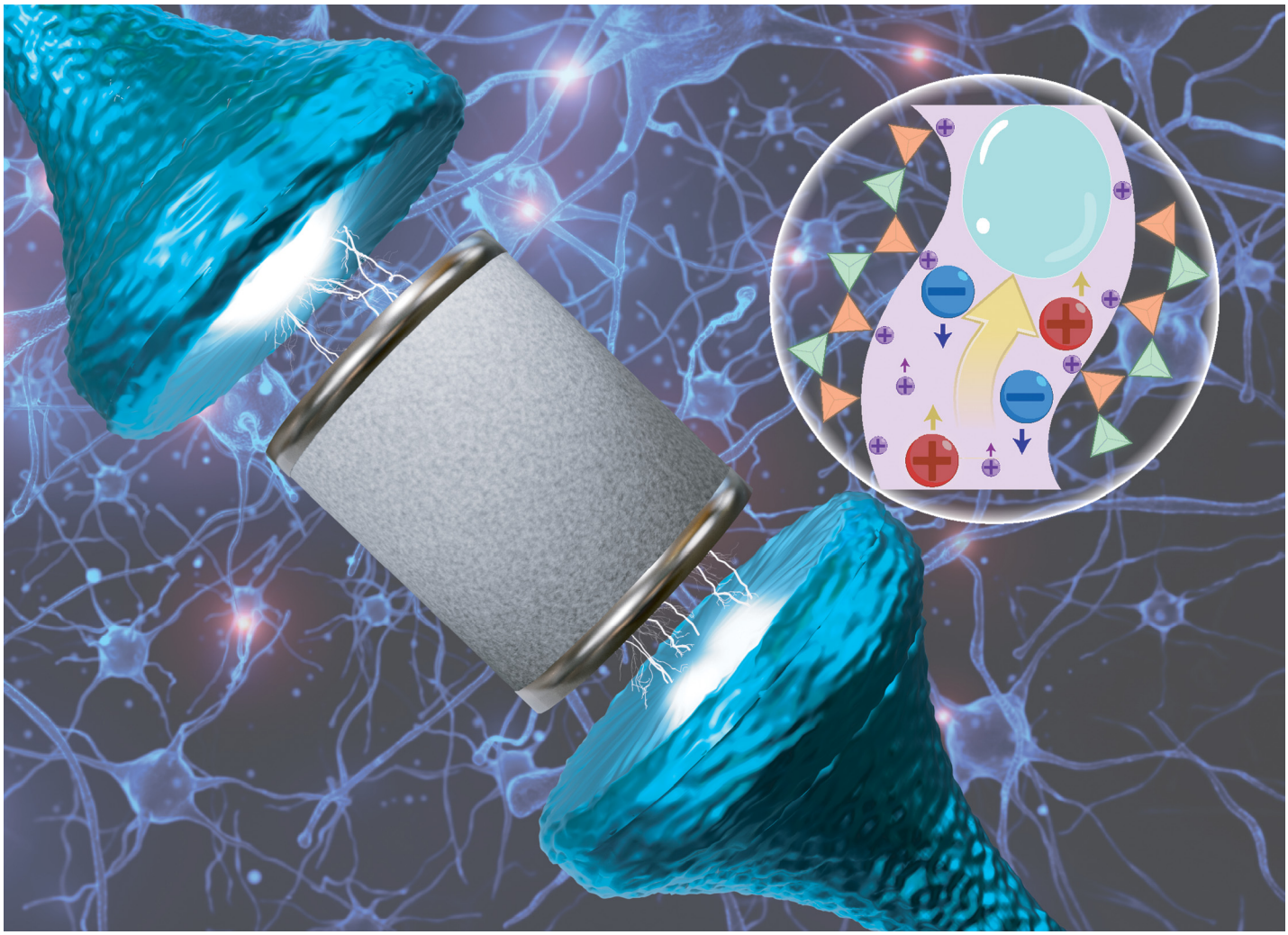

Showcasing collaborative research from the groups of Professors Caterina Lamuta (University of Iowa), Reza Montazami (Iowa State University) and Stephen A. Sarles (University of Tennessee)

Scaled-down ionic liquid-functionalized geopolymer memristors

Inspired by biological synapses, memristors are the functional units of neuromorphic computing. Low-cost geopolymer memristors have been fabricated at micron-scale for more enhanced applicability in neuromorphic computing. Devices were functionalized with ionic liquids, significantly improving their longevity and retention of resistive switching capabilities. A collection of synaptic plasticity properties were demonstrated, paving the way for their use in next-generation smart infrastructure. Background by onimate *via* Adobe Stock.

Image reproduced by permission of Mahmudul Alam Shakib from *Mater. Horiz.*, 2025, **12**, 4208.

As featured in:

See Stephen A. Sarles, Caterina Lamuta, Reza Montazami *et al.*, *Mater. Horiz.*, 2025, **12**, 4208.

ROYAL SOCIETY OF CHEMISTRY

rsc.li/materials-horizons

Registered charity number: 207890

Materials Horizons

ROYAL SOCIETY OF CHEMISTRY

COMMUNICATION

View Article Online
View Journal | View Issue

Open Access Article. Published on 13 May 2025. Downloaded on 3/6/2026 3:41:36 AM.
This article is licensed under a Creative Commons Attribution 3.0 Unported Licence.

Check for updates

Cite this: *Mater. Horiz.*, 2025, **12**, 4208

Received 6th February 2025,
Accepted 6th May 2025

DOI: 10.1039/d5mh00231a

rsc.li/materials-horizons

Scaled-down ionic liquid-functionalized geopolymer memristors†

Maedeh Ahmadipour, ‡[a] Mahmudul Alam Shakib, ‡[b] Zhaolin Gao,[b] Stephen A. Sarles, *[c] Caterina Lamuta*[b] and Reza Montazami *[ad]

Whereas most memristors are fabricated using sophisticated and expensive manufacturing methods, we recently introduced low-cost memristors constructed from sustainable, porous geopolymers (GP) at room temperature *via* simple casting processes. These devices exhibit resistive switching *via* electroosmosis and voltage-driven ion mobility inside water-filled channels within the porous material, enabling promising synaptic properties. However, GP memristors were previously fabricated at the centimeter scale, too large for space-efficient neuromorphic computing applications, and displayed limited memory retention durations due to water evaporation from the pores of the GP material. In this work, we overcome these limitations by implementing (i) an inexpensive manufacturing method that allows fabrication at micron-scale (99.998% smaller in volume than their centimeter-scale counterparts) and (ii) functionalization of GPs with EMIM$^+$ Otf$^-$ ionic liquid (IL), which prolonged retention of the memristive switching properties by 50%. This improved class of GP-based memristors also demonstrated ideal synaptic properties in terms of paired-pulse facilitation (PPF), paired-pulse depression (PPD), and spike time dependent plasticity (STDP). These improvements pave the way for using IL-functionalized GP memristors in neuromorphic computing applications, including reservoir computing, in-memory computing, memristors crossbar arrays, and more.

New concepts

This work introduces ionic liquid-functionalized micron-scale geopolymer memristors as a novel class of sustainable, low-cost, and scalable devices capable of both resistive switching and synaptic plasticity. Unlike conventional memristors, which require sophisticated and costly manufacturing techniques, we demonstrate a simple, room-temperature casting process that scales down GP memristors to 200 μm—with a 99.998% volume reduction compared to previously manufactured samples—while simultaneously extending their functional lifespan. The introduction of EMIM$^+$ Otf$^-$ IL addresses the inherent challenge of moisture loss in GP structures, preserving memristive switching behavior for over three weeks—50% longer than pristine GP devices. Additionally, IL-functionalization reduces activation voltage requirements from 5 V to 0.3 V, significantly lowering power consumption. These IL-functionalized GP memristors also exhibit ideal synaptic behaviors such as paired-pulse facilitation, paired-pulse depression, and spike-timing dependent plasticity, demonstrating their potential for applications in energy-efficient neuromorphic computing. The multifunctional properties of GP (that, besides synaptic behavior, also present a piezoresistive and piezoelectric effect), position these inexpensive materials as a promising candidate for intelligent structural health monitoring (SHM), enabling the integration of real-time sensing, adaptive learning, and autonomous damage detection within a single system.

Introduction

The performance and architecture of the biological brain have puzzled scientists for centuries.[1] Housed inside the thick skull, a mammalian brain can outperform a supercomputer, although it runs at only ∼20 watts.[2] The advancements in modern science, particularly in silicon-transistor technology, have significantly enhanced the performance and computational power of computing hardware. However, the Von Neumann architecture that they are built upon mandates the segregation of memory storage and processing units, which severely constrains the processing speed of the computers.[3] Furthermore, the dimensions of silicon-based chips, following Moore's law, have been reduced to such a degree that further miniaturization of transistor components may soon reach a fundamental limit imposed by the atomic size of silicon.[4] The memristor is the smallest unit of brain-inspired computing hardware that has the potential to address the bottleneck in Von Neumann architecture and the scaling limitations imposed by Moore's law. Possessing both analog and digital memory, certain

[a] *Department of Mechanical Engineering, Iowa State University, Ames, Iowa 50011, USA. E-mail: reza@iastate.edu*
[b] *Department of Mechanical Engineering, College of Engineering, University of Iowa, Iowa City, Iowa 52242, USA. E-mail: caterina-lamuta@uiowa.edu*
[c] *Department of Mechanical, Aerospace, and Biomedical Engineering, University of Tennessee, Knoxville, Tennessee 37916, USA. E-mail: ssarles@utk.edu*
[d] *Department of Agricultural and Biosystems Engineering, Iowa State University, Ames, Iowa 50011, USA*

† Electronic supplementary information (ESI) available. See DOI: https://doi.org/10.1039/d5mh00231a

‡ These authors contributed equally.

This journal is © The Royal Society of Chemistry 2025

Open Access Article. Published on 13 May 2025. Downloaded on 3/6/2026 3:41:36 AM.
This article is licensed under a Creative Commons Attribution 3.0 Unported Licence.

memristors have the potential to integrate memory storage and computational processing within a single device. Moreover, some are also compatible with traditional CMOS fabrication technology. Many different material systems have been considered to develop memristors; these include both synthetic and naturally-available organic and inorganic materials such as metal oxides, ceramics, perovskites, and biomaterials such as proteins, saccharides, and DNA.[5–9] Memristor devices are usually fabricated at micrometer or nanometer length scales *via* expensive and sophisticated manufacturing techniques such as pulsed laser deposition (PLD), electrochemical deposition, and photolithography.[9–12]

Activity-dependent memory in memristors is attributed to a stimulus-induced change in the conductance of the material and its ability to remember the current that flows through it (that is usually visualized *via* pinched hysteresis in a current–voltage plot).[13,14] Different switching mechanisms (*i.e.*, the time-changing conductance behavior) have been observed for memristors obtained from other material systems.

Geopolymers (GPs) are amorphous ceramic materials synthesized by alkaline activation of natural aluminosilicate precursors (*e.g.*, metakaolin, fly ash). First proposed by Davidovits in 1978,[15] GPs have been mainly studied as an eco-friendly alternative to ordinary Portland cement. Their status has evolved from traditional construction materials to advanced multifunctional ceramics following our recent discovery of their piezoelectric[16,17] and piezo resistive[18] properties, which arise from the transport of solvents and ions within their porous architecture under applied mechanical loads. Building on these findings, we have also demonstrated that GPs also represent a new category of low-cost memristors. Manufactured at room temperature *via* simple cold casting, GP memristors showed all the characteristic fingerprints of memristors along with promising synaptic properties. A novel switching mechanism involving voltage-driven electroosmosis and ion mobility inside the hydrated pores of GP was also demonstrated.[19,20]

However, GP memristors developed in our previous works were centimeter-scale devices with limited longevity ($\sim$2 weeks) of memristive properties due to water evaporation from their pores, hindering their integration into neuromorphic systems. To address these limitations, we present two key innovations: (1) micron-scale fabrication of GP memristors *via* a scalable and low-cost process to reduce device volume and (2) Functionalization of GPs with ionic liquid (IL) to enhance device longevity.

Being fully ionic compounds, ILs exhibit ultra-low vapor pressures[21] and melting points below 100 °C.[22] Moreover, certain ILs demonstrate good air stability[22] and thermal stability[23] and are cost-effective to synthesize, making them advantageous for enhancing device stability and longevity. The first IL-based memory device was proposed in 2010 and consisted of a protic-IL gated electric double layer (EDL) transistor that achieved proton memory function *via* surface hydrogenation.[24] Two years later, another study demonstrated non-volatile memory in a device made of graphene oxide (GO) functionalized with an IL.[25] These works inspired a synaptic transistor that could mimic synaptic plasticity and memory retention,[26] which opened the gateway for IL-based neuromorphic devices. To date, several studies have been conducted to fabricate IL-based memristors and artificial synapses. Provided in Table 1 is a representative list of the current state-of-the-art in IL-based neuromorphic devices, highlighting the main properties observed for each device. In many of these devices, IL occupies channels and capillary tubes across millimeter,[27,28] micrometer,[21,29,30] and nanometer[25,26,31–34] scales. Some devices have employed alternative methods, such as sandwiching a layer of IL.[35] For instance, Suga *et al.* utilized preferential phase segregation of IL into spherical and inverse spherical nanotemplates.[36] However, all existing studies required intensive procedures to fabricate channels, pores, or capillaries for IL to enable charge transport.

In this study, we employed a micro-molding approach to scale down GP memristors to the micron scale, achieving a 99.998% reduction in device volume compared to their centimeter-scale predecessors. In addition, we incorporated 1-ethyl-3-methylimidazolium trifluoromethanesulfonate ($EMIM^+$ Otf^-) IL into the micro- and nano-channels of the naturally porous GP as a non-volatile liquid phase to facilitate ion mobility and mitigate evaporation while preserving device functionality. The ultra-low volatility of $EMIM^+$ Otf^- significantly enhanced the longevity of the GP memristors, as demonstrated by greater stability of the pinched hysteresis in their *I–V* characteristic plot over three weeks of experimental testing. We demonstrated that these improved devices require activation voltages as low as 0.3 V and can emulate synaptic behaviors, including paired-pulse facilitation (PPF), paired-pulse depression (PPD), and spike-timing-dependent plasticity (STDP). The enhancement in device longevity, coupled with approximately four orders of magnitude reduction in device volume, highlights the potential of this low-cost material system for the efficient and cost-effective fabrication of neuromorphic computing devices.

The unique combination of electro-mechanical and electrochemical properties enables GPs to function simultaneously as structural materials, sensors, and neuromorphic devices. Their direct piezoelectricity[16,17] enables force sensing, while their memristive properties support resistive switching and synaptic plasticity emulation. This novel multifunctionality makes GPs ideal for advanced applications such as structural health monitoring (SHM) systems, where they can integrate sensing, real-time data processing, and damage prediction within a single material platform.[41–43] By combining sensing capabilities with neuromorphic functionality, GPs pave the way for next-generation intelligent systems with adaptive learning, real-time decision-making, and efficient integration into smart infrastructure.

Materials and methods

Materials

Low alkaline Na_2SiO_3 powder was obtained from Chemicalstore (Clifton, NJ, USA). NaOH pellets were sourced from Fisher Chemical (Pittsburg, PA, USA). Metakaolin was purchased from Carbo (Houston, TX, USA). 1-Ethyl-3-methylimidazolium trifluoromethanesulfonate ($EMIM^+$ Otf^-) (CAS# 145022-44-2, M_w = 260.23 g mol^{-1}) was procured from Sigma Aldrich

Open Access Article. Published on 13 May 2025. Downloaded on 3/6/2026 3:41:36 AM.
This article is licensed under a Creative Commons Attribution 3.0 Unported Licence.

Table 1 A representative list of IL-based neuromorphic devices

Ionic liquid	Device structure	Neuromorphic properties	Ref./year
IL doped with weak Brønsted acid	Dielectric layer of EDL transistor functionalized with IL	Proton memory	24 2010
NMP and DMF	Graphene oxide covalently functionalized with IL	Non-volatile memory	25 2012
Generalized	Perovskite $SmNiO_3$ (SNO) channel	Potentiation–depression, spike-timing-dependent-plasticity (STDP)	26 2013
Poly [VBIT]	Poly-IL layer sandwiched between active layer and electrode	Resistive switching, high retention time, stable switching	35 2015
TEMPO	Preferential phase segregation of IL into spherical and inverse spherical nanotemplates	Resistive switching memory	36 2015
BMIM-TFSI	IL-Based polymer nanocomposites	Volatile resistive switching,	37 2016
[BMIM][BF_4]	Nano-channel	Resistive switching	31 2017
[BMIM][Br]	Sample tube filled with IL. Copper wires inserted from two extremities as electrodes.	Resistive switching, Uniform endurance	27 2019
DEME-TFSI	NiO layer pre-treated with IL under positive voltage.	Resistive memory switching, uniform operation voltage	38 2019
Generalized	Liquid interface between IL and immiscible KCl inside PDMS nanochannels.	Synaptic plasticity for hand-written digit recognition	32 2019
DEME-TFSI	Anthocyanin as active layer and functionalized by graphene and IL	Battery-like self-selecting behavior in memristor arrays	39 2021
[BMIM][Tf_2N]	Microfabricated pore filled with IL sandwiched between Pt and Cu electrodes.	Controllable data-volatility	21 2021
DEME-TFSI	IL droplet used to create a heterojunction for transport of carriers	True random number generator	40 2021
BMIM $FeCl_4$ and H_2O	PDMS mold with milli- and micro-channel filled with IL	Multistate resistive switching, synaptic behavior	28–30 2022
[MMIm][Cl]	IL in a capillary tube	Temporary memory	33 2023
[MMIm][NO_3]: H_2O	IL in a capillary tube	Resistive switching, Synaptic plasticity	34 2024
[EMIM][Otf]	Naturally available micro- and nano-pores of geopolymer treated with IL.	Memristive switching, synaptic plasticity, paired-pulse facilitation (PPF), paired-pulse depression (PPD), STDP	This work

(St. Louis, MO, USA). Kapton film of 140 μm thickness was sourced from Addicore (San Diego, CA, USA). Leitsilber silver adhesive was bought from Ted Pella Incorporation (Redding, CA, USA).

Sample fabrication

As shown in Fig. 1a, the fabrication of geopolymer samples involved a cost effective and scalable process consisting of material preparation, micro-mold casting, and post-curing treatments. Unlike conventional memristor fabrication techniques that rely on high-vacuum deposition methods,[44–46] complex lithographic patterning,[47] or multi-step etching,[48] this approach enables straightforward device fabrication using accessible materials and ambient processing conditions. This section outlines, in detail, steps taken to ensure precise composition and quality fabrication of devices prepared and used for subsequent experiments. To prepare the geopolymer slurry, 1.92 g of Na_2SiO_3 powder was dissolved in 1.81 g deionized (DI) water and maintained on a magnetic stirrer at 400 rpm and 30 °C for 1 hour. This solution was then mixed with 0.42 g of NaOH pellets for 5 hours at room temperature, continuing to stir at 400 rpm and 30 °C to ensure the desired consistency. Lastly, 2.66 g of Metakaolin was added to the solution and stirred at 1150 rpm for 10 minutes.

A laser beam was used to create circular cavities of 200 μm, 500 μm, and 1000 μm diameters on polyimide (Kapton) film of 140 μm thickness to be used as molds for GP devices. Kapton film was used as a mold to define the shape and dimensions of the geopolymer during curing. It remains in place but does not contribute to the electrical performance of the device. The laser microperforation was performed using an ORTUR Laser Master 2 Pro S2. The laser power was set to 100% and the speed to 500 mm min^{-1} to perforate circular cavities. The laser microperforation was performed in three, five, and fifteen consecutive runs at the specified power and speed for each diameter to prevent overheating and thermal decomposition of the polyimide film. The circular cavities were then examined using a digital microscope to verify the diameter and ensure the absence of any polyimide decomposition. The molds were then cleaned with methanol and pressurized water to remove any residues. The geopolymer slurry was poured into each mold and left to dry at room temperature for 2–3 minutes. After the drying period, any excess slurry around the edges of the mold was removed using a squeegee. The samples were then cured in an oven at 60 °C for 1 hour and kept at room temperature overnight. Unlike traditional high-temperature sintering or vacuum-assisted deposition methods, this process is performed at ambient temperature, reducing fabrication complexity and cost.[49] Functionalization was achieved by adding a small drop (5 μL) of $EMIM^+$ Otf^- IL on each end of geopolymer samples using a micropipette. After approximately 1 minute, any excess

Open Access Article. Published on 13 May 2025. Downloaded on 3/6/2026 3:41:36 AM.
This article is licensed under a Creative Commons Attribution 3.0 Unported Licence.

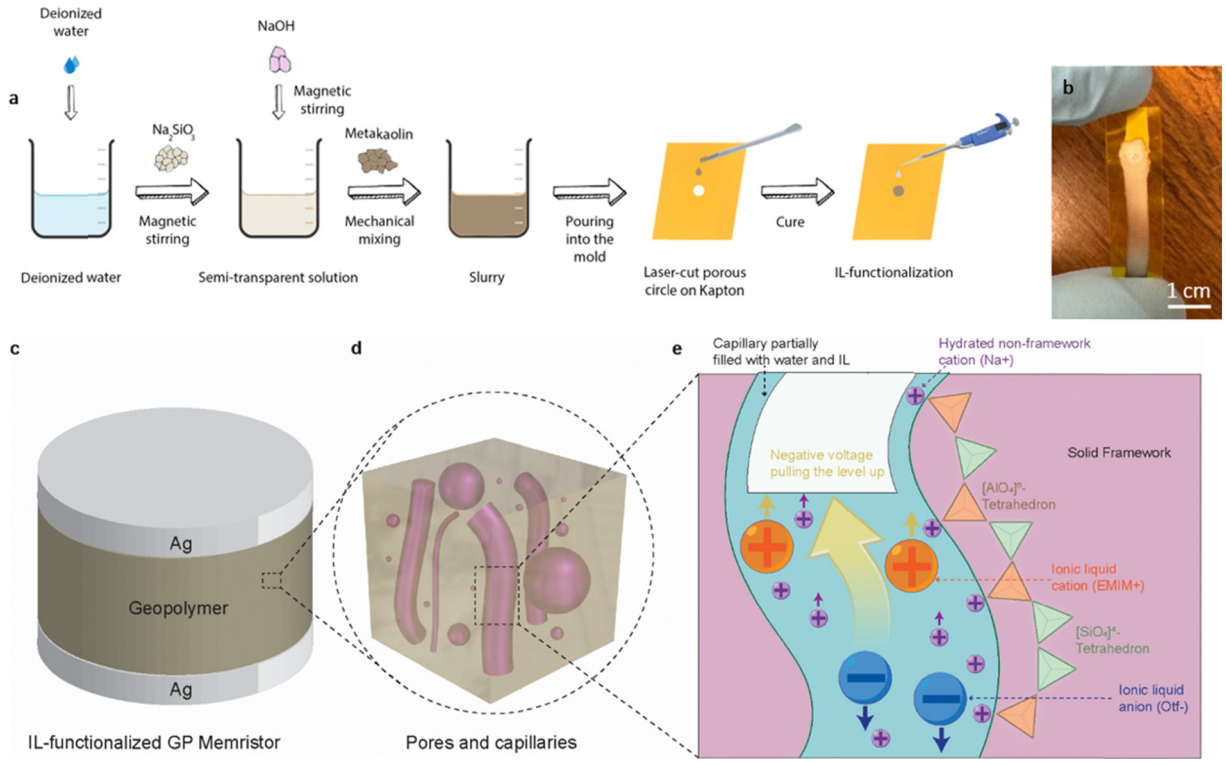

Fig. 1 (a) A schematic representation of the fabrication process for a micron-scale IL-functionalized GP memristor; (b) an optical image of an actual IL-functionalized GP device (thickness = 140 μm and diameter = 1000 μm); (c) structure of an IL-functionalized GP memristor. The memristor consists of geopolymer material sandwiched between two Ag electrodes; (d) illustration of a magnified view of tortuous capillaries and pores; (e) schematic illustration of electroosmosis driven memristive mechanism in an IL-functionalized GP memristor.

IL was removed using a Kimwipe. Following a 30-minute equilibration period at room temperature, a conductive silver adhesive was applied to each end of the IL-functionalized geopolymer samples using the applicator brush provided with the adhesive. The samples were then placed in a fume hood for 1 hour to facilitate the drying of the silver adhesive.

Device characterization

The *I–V* hysteresis characteristics of GP memristors were evaluated using an apparatus comprising a function generator, an oscilloscope, and an ammeter. The function generator was used to apply a sinusoidal waveform across the top and bottom electrodes of the device as the amplitude of the waveform and the drawn current were synchronizingly measured and recorded on the oscilloscope and ammeter. Cyclic voltammetry (CV) experiments were carried out using Biologic SP-300 potentiostat. Two potentiostat leads were connected to the device's top and bottom electrodes. Conductance modulation of GP devices in response to repeated voltage pulses was measured employing the chronoamperometry mode. For SRDP, PTP, PPF, and PPD characterization, a single measurement channel of Biologic SP-300 potentiostat was utilized where two probes of the channel were connected to the top and bottom electrodes of the device, as shown in Fig. S1 (ESI†). For paired pulses in STDP characterization, two measurement channels were utilized. The top and bottom electrodes of the device were regarded as the pre- and post-synaptic locations, respectively, and were connected to the two channels of the potentiostat, as shown in Fig. S2 (ESI†).

Materials characterization

An FEI Quanta-FEG 250 scanning electron microscope operated in backscattered electron (BSE) mode was utilized for the SEM imaging. An Oxford Instruments Aztec energy-dispersive spectrometer equipped with an X-Max 80 light-element detector (80 mm^2 active area) was used to perform energy-dispersive X-ray spectroscopy (EDX). An X-ray count rate of ∼15 kcps was used, and X-ray maps of 256 × 244 pixels were collected for 10 minutes. Inductively coupled plasma-mass spectroscopy (ICP-MS) was employed to analyze the ionic composition of the entrapped solution (pore solution) within the geopolymer matrix. Pore solution was prepared for the spectroscopy technique following a previously reported method.[50,51] Geopolymer memristor samples without silver electrodes were crushed with mortar and pastel to obtain a powder. This powder was sieved using a 150 μm sieve. Then, 0.1 gram of the sieved powder was added to 400 ml of DI water and heated on a hot plate stirrer at 100 °C for 4 hours; then left to cool overnight at room temperature. Five samples of pore solution, each of 10 ml, were prepared for ICP-MS tests. An Agilent 7800 Quadrupole ICP-MS was used to test the samples. Each sample was analyzed for traces of Na^+, Mg^{2+}, and Fe^{3+} ions.

Open Access Article. Published on 13 May 2025. Downloaded on 3/6/2026 3:41:36 AM.
This article is licensed under a Creative Commons Attribution 3.0 Unported Licence.

Curve fitting

Curve fittings for PPF, PPD, PTP, and PPF indices, as well as Hebbian learning, were performed using MATLAB 2024a and Simulink.

Results and discussions

Memristive fingerprints and long-term stability

Micron-scale geopolymer devices were fabricated to address limitations in previous designs, which were primarily constructed at the millimeter scale.[19,20] This approximately four orders of magnitude—more precisely, 61 600× —reduction in device volume enhances the suitability of the devices for microelectronics and other applications where speed and energy efficiency are critical. Reducing the device volume is expected to enhance operational efficiency, as smaller geometries enable faster ionic transport and more efficient charge dynamics. Fig. 1a presents a schematic representation of the fabrication process for micron-scale IL-functionalized geopolymers, along with an optical image of a device fabricated in the laboratory (Fig. 1b). Fig. 1c shows the device structure of a typical IL-functionalized GP memristor, where the two Ag electrodes sit on the top and bottom of the bulk GP material. Pores and capillaries are naturally created during the curing process of GP materials, as shown in Fig. 1d. Fig. 1e schematically illustrates how pores are partially filled with pore solution and IL, forming a fluid column within the pore, surrounded by a solid framework. This framework is composed of $[AlO_4]^{5-}$ and $[SiO_4]^{4-}$ tetrahedrons, shown in orange and green, respectively, connected through shared oxygen atoms. The pore wall is negatively charged by the negative charges of aluminum tetrahedrons. The Na^+ ions (in purple) of the pore solution and $EMIM^+$ cations of IL are attracted by the negatively charged pore wall, creating an electrical double layer at the pore wall–solution interface. When an external voltage is applied to the GP memristor, the positively cations, such as Na^+ and $EMIM^+$, move within the pores toward the cathode. This ionic movement induces an electroosmotic flow that drags the liquid within the pore in the direction of the ion migration. The resulting redistribution of ions and liquid alters the ionic environment within the pores, which dynamically modulates the resistance of the IL-functionalized GP memristor and contributes to its memristive behavior. The porous structure of geopolymer memristors, including pore size distribution and tortuosity, has been extensively characterized in our previous work[19] using N_2 BET analysis and Mercury Intrusion Porosimetry (MIP).

Seven devices were tested for each size category (1000 μm, 500 μm, and 200 μm diameter) to ensure reproducibility. A continuous sinusoidal waveform of 5 V amplitude and 0.01 Hz frequency was used to probe the current–voltage relationship for each device, while the induced current was recorded to study the three memristive fingerprints described by Adhikari *et al.*[52] These fingerprints include (1) the presence of a pinched hysteresis loop in the *I–V* plane when driven by a bipolar signal, (2) a decrease in the hysteresis lobe area as frequency increases, and (3) the eventual collapse of the hysteresis loop to a single-valued function at high frequencies.[13] As shown in Fig. 2b, the *I–V* plot of the IL-functionalized geopolymer sample confirms that it exhibits all three functional fingerprints of a memristor.[53] The figure exhibits a pinched hysteresis loop, verifying the first characteristic when the sample is subjected to a bipolar signal. Furthermore, the gradual reduction in the hysteresis lobe area is evident as the frequency increases, demonstrating the second fingerprint. At the highest frequency (0.5 Hz), the hysteresis loop converges into a linear response, indicating the transition to a non-hysteretic state, thus validating the third fingerprint.

In the brain, synaptic connections adapt based on the frequency of neural signals, where low-frequency stimuli can strengthen synapses through facilitation, while high-frequency stimuli may lead to a loss of this dynamic adaptability.[54,55] Understanding how the memristor's *I–V* characteristics shift with frequency reveals how GP memristors can emulate frequency-dependent synaptic plasticity in neuromorphic systems.[55–58] The *I–V* characteristics of an IL-functionalized GP device under

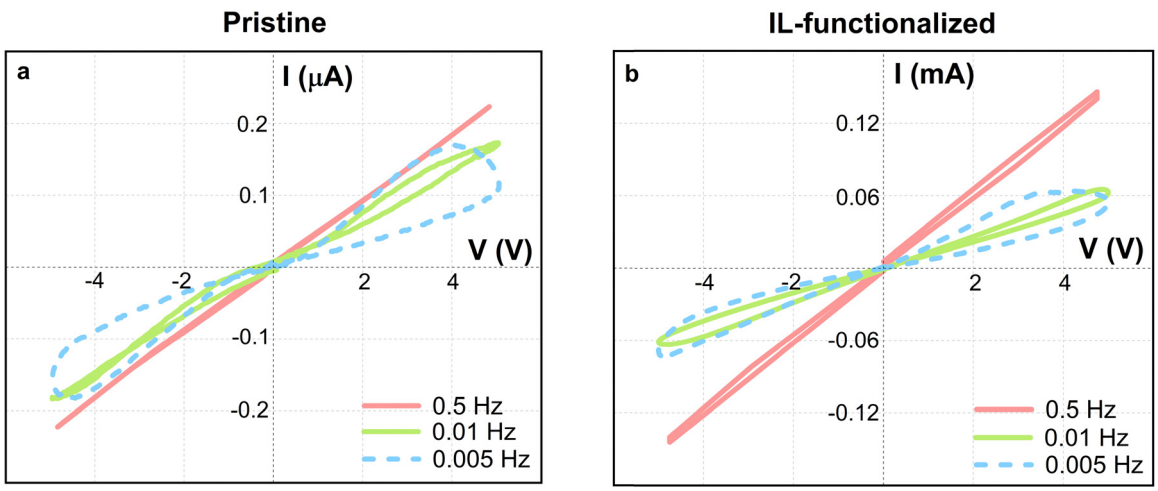

Fig. 2 *I–V* graphs under sinusoidal waveforms at varying frequencies (0.005 Hz, 0.01 Hz, and 0.5 Hz) for (a) pristine and (b) IL-functionalized GP devices. All tests were conducted on devices with ϕ = 1000 μm.

 This journal is © The Royal Society of Chemistry 2025

Open Access Article. Published on 13 May 2025. Downloaded on 3/6/2026 3:41:36 AM.
This article is licensed under a Creative Commons Attribution 3.0 Unported Licence.

varying frequencies are shown in Fig. 2b, demonstrating a broad pinched hysteresis loop at low frequencies, which is indicative of a dominating capacitive behavior. At low frequencies, Na^+ and $EMIM^+$ cations have sufficient time to migrate and form conductive pathways, leading to the creation of ionic space-charge regions near Ag electrodes. This slow ion movement results in a dynamic balance between ion migration and relaxation, causing the broad hysteresis loop, where energy is stored in the system. This behavior mimics synaptic facilitation, where infrequent signals allow for greater synaptic strength due to neurotransmitter accumulation. As the frequency increases, the hysteresis loop narrows and eventually disappears, transitioning the memristor into a more resistive regime.[59] At higher frequencies (0.5 Hz), ion migration becomes less synchronized with the rapid voltage changes; however, it still plays a crucial role in maintaining conductivity. This behavior might be influenced by the rate of electroosmotic flow within the device's pores, which could be the rate-limiting factor at higher frequencies. Interestingly, the increased average slope of *I–V* graphs at higher frequencies suggests enhanced conductivity. This phenomenon could be attributed to a more uniform distribution of charge carriers facilitated by the rapid switching, potentially reducing localized resistances and increasing overall conductance.

To further understand the impact of the IL on device behavior, the *I–V* responses of micron-scale pristine GP samples at varying frequencies were analyzed, as shown in Fig. 2a. Similar to the IL-functionalized GP devices, pristine GP samples exhibit frequency-dependent behavior, with a broad hysteresis loop at low frequencies and a more linear response at higher frequencies. However, the pristine GP devices show less pronounced capacitive behavior compared to the IL-functionalized samples, indicating that the IL enhances the frequency-dependent response. This enhancement is attributed to the $EMIM^+$ and Otf^- ions of the IL, which are introduced to the GP matrix and provide mobile charge carriers, thereby increasing the overall conductivity by creating additional charge pathways. In both the pristine (Fig. 2a) and IL-functionalized (Fig. 2b) GP samples, the cycle progresses in a clockwise direction from the origin in the first quadrant, then moves counterclockwise toward the third quadrant, and finally returns to the origin, exhibiting a cross-quadrant behavior.[19,60] This behavior contrasts with previous studies on larger geopolymer devices with a lower diameter/thickness ratio (ϕ/h = 0.51), which exhibited a counterclockwise direction in the first quadrant.[19] The micron-sized GP devices have a higher ϕ/h ratio (ϕ/h = 1.43), meaning they are relatively wide rather than thick. This size reduction appears to influence hysteresis direction, as the increased surface-to-volume ratio enhances edge effects and ionic interactions near the electrodes, leading to a stronger space-charge formation in the first quadrant.

Fig. 3 presents the *I–V* characteristics of IL-functionalized and pristine micron-scale geopolymer devices with varying diameters and constant thickness (h = 140 μm), measured immediately after fabrication and then again after one week of aging. The data reveals a distinct difference in behavior between IL-functionalized and pristine devices, particularly in terms of their stability and memristive properties. For the IL-functionalized GP devices, shown in Fig. 3a–c, the immediate *I–V* plots exhibit well-defined pinched hysteresis loops for all diameters (1000 μm, 500 μm, and 200 μm). The observed loops confirm non-volatile memristive behavior, with relatively large lobe areas that signify the ability to retain state-dependent

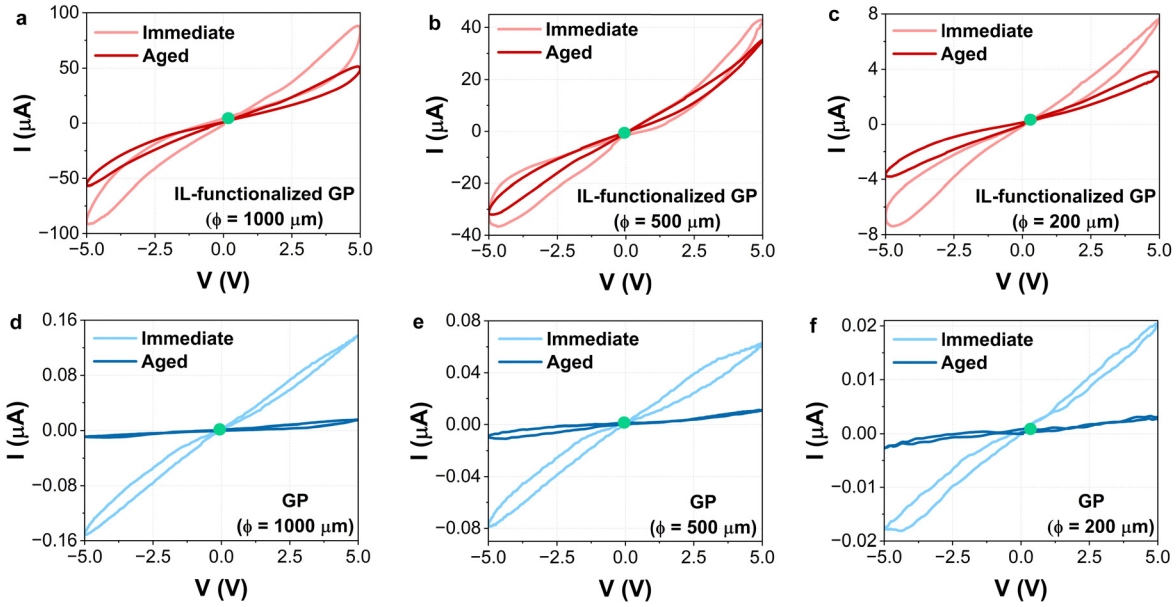

Fig. 3 *I–V* characteristic plots of IL-functionalized and pristine micron-scale geopolymer devices with various diameters (d) and a constant thickness (h = 140 μm), measured immediately after fabrication and after one week of aging. (a) IL-functionalized geopolymer device with ϕ = 1000 μm; (b) IL-functionalized geopolymer device with ϕ = 500 μm; (c) IL-functionalized geopolymer device with ϕ = 200 μm; (d) pristine geopolymer device with ϕ =1000 μm; (e) pristine geopolymer device with ϕ = 500 μm; and (f) pristine geopolymer device with ϕ = 200 μm.

Open Access Article. Published on 13 May 2025. Downloaded on 3/6/2026 3:41:36 AM.
This article is licensed under a Creative Commons Attribution 3.0 Unported Licence.

electrical responses. After one week of aging, the IL-functionalized devices continue to exhibit pinched hysteresis loops, although the lobe areas are noticeably smaller, indicating a reduction in memristive performance due to aging. Nonetheless, the consistent presence of pinched hysteresis in all seven fabricated IL-functionalized samples across all diameters confirms that the addition of IL significantly stabilizes and preserves the memristive properties of the devices over time.

In contrast, the pristine GP devices, as shown in Fig. 3d–f, display a more short-lived response. Immediately after fabrication, devices demonstrate pinched hysteresis loops, indicative of memristive behavior, though with smaller lobe areas compared to their IL-functionalized counterparts. After one week of aging, the majority of pristine GP devices lose their pinched hysteresis loops and, consequently, their memristive properties. The aged pristine devices typically exhibit elliptic loops with no pinching, indicative of non-memristive behavior. This transformation is attributed to changes in the internal network of liquid-filled channels, which have diminished due to the evaporation of residual water. This evaporation also contributes to the noisy appearance of the *I–V* plots in aged pristine samples. The results demonstrate that the degradation of pristine devices is rapid, particularly for smaller diameters. For example, out of ten fabricated pristine devices for each diameter, only two 1000 μm and 500 μm samples and one 200 μm sample retained pinched hysteresis loops after aging, while the remainder transitioned to non-memristive behavior. The absence of IL in these samples likely accelerates the loss of electrical performance. All seven IL-functionalized GP sample results and all ten pristine GP sample results, both immediate and after one week of aging, are shown in Fig. S3 and S4 (ESI†).

To further substantiate the role of IL in preserving the memristive properties of the geopolymer devices, the seven IL-functionalized samples were re-evaluated after three weeks of aging. The results, presented in Fig. S5 (ESI†), confirm that all samples retained pinched hysteresis behavior after 21 days, demonstrating the stability and performance of IL-functionalized devices over time. Enhanced durability can be attributed to the intrinsic environmental stability of ILs, which minimize the structural changes typically induced by aging, and their pivotal role in facilitating the availability and mobility of ionic species within the geopolymer matrix. These factors collectively contribute to the sustained memristive properties observed in IL-functionalized devices, further validating the efficacy of IL integration in improving the long-term electrical performance of geopolymer-based memristors.[37] In the biological context, this is akin to the ability of synapses to maintain their strength over long periods, ensuring reliable device longevity. In contrast, pristine devices exhibit more rapid degradation, reflecting less stable behavior and shorter device longevity capabilities, which is less desirable for long-term neuromorphic applications. The results are consistent with previous studies, which have demonstrated that reducing the amount of freely moving ions from IL or omitting IL in memristor samples leads to a smaller hysteresis area, indicating weaker memristive performance.[27]

The conductivity switching behavior in geopolymer memristors is influenced by several factors, including device size and pore structure. Larger devices exhibit higher current outputs due to their increased maximum pore radius, which facilitates greater ion mobility within the hydrated pores. This is supported by fitting the experimental results using our electroosmosis-based model,[19] which shows that smaller values of the maximum pore radius result in reduced output currents for the same input voltage (see Fig. S6, ESI†). Additionally, the number of conductive paths (ion channels) scales with device size. Larger devices contain more pores, leading to a higher number of ion channels and, consequently, greater overall conductivity. This is evident in Fig. 3, where the current response in larger devices (*e.g.*, 1000 μm diameter) reaches ∼100 μA, while in smaller devices (*e.g.*, 200 μm diameter), it is reduced to ∼8 μA for IL-functionalized GP devices. Similarly, the current response reduces from ∼0.14 μA to ∼0.02 μA for pristine GP samples.

Based on the analysis of seven IL-functionalized and ten pristine GP samples, the lobe areas were evaluated immediately after fabrication and after one week of aging, as shown in Fig. 4a and b. The pristine geopolymer samples exhibit significant degradation across all diameters, with aged lobe areas showing substantial reductions compared to their immediate values. Specifically, the lobe areas decrease by 89.63%, 88.11%, and 95.84% for 1000 μm, 500 μm, and 200 μm samples, respectively, with many losing their pinched hysteresis properties entirely (Fig. 4a). In contrast, the IL-functionalized geopolymer samples, shown in Fig. 4b, demonstrate markedly greater resilience, retaining a larger fraction of their initial lobe areas after aging. The reductions in lobe areas for the IL-functionalized samples are 71.9%, 75.6%, and 65.6% for the same diameters, with all preserving their memristive properties. This represents a 30.24% improvement in longevity compared to the pristine samples, where the maximum device longevity is less than 12%. In both cases, the loss of lobe area is attributed to water evaporation. The incorporation of IL reduces the impact of aging, as evidenced by the relatively consistent lobe areas in aged samples, especially in smaller devices (200 μm and 500 μm). The larger diameter samples (1000 μm) exhibit a slightly greater reduction in lobe area compared to smaller diameters, which may be attributed to greater initial water retention in larger volumes. Fig. 4c demonstrates the enhanced temporal retention of memristive properties in IL-functionalized samples, as indicated by their higher aged-to-immediate lobe area ratios (%) compared to pristine samples. While pristine samples exhibit low ratios across all diameters, reflecting rapid degradation, IL-functionalized devices maintain higher ratios, particularly for smaller diameters, demonstrating better retention of memristive behavior over time. These findings confirm the role of IL in mitigating structural and ionic degradation, making IL-functionalized devices more reliable for long-term applications. Additionally, a comparative analysis of the lobe areas in both experimental and model results[19,20] further reinforce the relationship between the pore radius and conductivity switching behavior. The electroosmosis-based model describes ion transport in partially hydrated geopolymer pores, where

 This journal is © The Royal Society of Chemistry 2025

Open Access Article. Published on 13 May 2025. Downloaded on 3/6/2026 3:41:36 AM.
This article is licensed under a Creative Commons Attribution 3.0 Unported Licence.

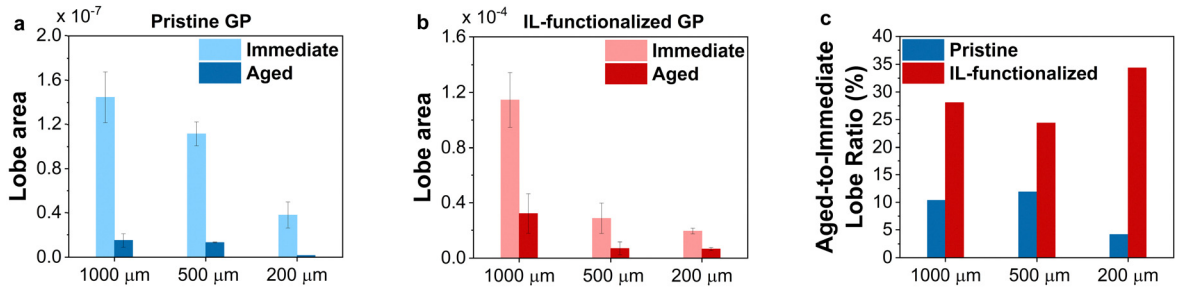

Fig. 4 Comparative analysis of the lobe area and temporal evolution of pristine and IL-functionalized geopolymer devices across varying diameters (1000 μm, 500 μm, 200 μm); (a) and (b) lobe areas measured immediately after fabrication and after one week of aging for pristine and IL-functionalized devices. Error bars represent the standard error of the population; (c) ratio of aged-to-immediate lobe area (%) for pristine and IL-functionalized devices, demonstrating enhanced temporal longevity in IL-functionalized devices.

conductivity switching is governed by electroosmosis within the pores and capillaries. The model predicts that as pore radius decreases, ion mobility is restricted, leading to reduced conduction and a corresponding decrease in lobe area (see Fig. S7, ESI†). This trend, observed consistently in both experimental and model predicted results, validates the role of pore size in governing memristive switching behavior and further supports the electroosmosis-based model.

Memristor devices are often valued for their ability to operate at low voltages, a feature that reduces power consumption and enhances compatibility with neuromorphic computing applications. To explore this aspect further, the IL-functionalized micron-scale geopolymer devices were tested under a reduced voltage to assess their functionality at lower activation thresholds. As shown in Fig. 5, even at low potentials of 1 V, 0.5 V, and 0.3 V, the IL-functionalized devices maintained a clear pinched hysteresis loop. In contrast, pristine micron-scale GP devices did not exhibit a pinched hysteresis loop under the same low-voltage conditions. Our findings suggest that reducing device volume from an initial volume of 270.92 mm^3 to 0.11 mm^3 and functionalization with IL are critical in maintaining the device's performance at lower activation thresholds. Compared to cm-scale devices, which require a minimum activation voltage of 5 V,[19,20] micron-scale IL-functionalized devices can operate at 0.3 V, significantly reducing energy and power consumption.

Contribution of silver oxidation on the memristive properties

A key issue in the performance of geopolymer memristors is the oxidation of silver at the electrode–geopolymer interface. While silver oxidation is a known electrochemical phenomenon, its influence on the memristive properties of geopolymers remains unclear. A series of characterization techniques, including SEM, EDX, and CV were employed to investigate the structural and electrochemical changes associated with Ag oxidation in both pristine and IL-functionalized geopolymer samples.

Initially, SEM imaging (Fig. 6) was used to examine the microstructure of the top surface of IL-functionalized geopolymer samples. As shown in Fig. 6(a)–(c), the SEM images reveal a granular and uneven surface morphology. This uneven surface is consistent with geopolymers' inherent porous structure. The accompanying EDX elemental maps (Fig. S10, ESI†) provide evidence of the distribution of S and F, key components of the $EMIM^+$ Otf^-, on the surface of GP. The SEM images in Fig. 6(d)–(g) show samples with a layer of silver adhesive applied to the geopolymer before testing (*i.e.*, before applying an electrical voltage). After testing the samples, significant changes are evident in the microstructure, as shown in Fig. 6(h)–(l). A comparison between Fig. 6d and h highlights differences between the untested and tested samples. Fig. 6g and k reveal morphological changes before and after electrical stimulation. In Fig. 6k, crystal-like

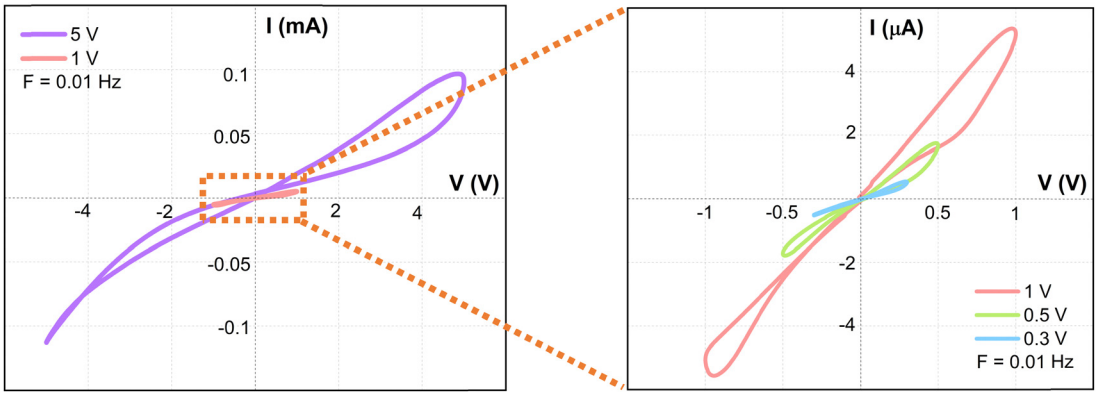

Fig. 5 *I*–*V* plot of an IL-functionalized geopolymer sample (ϕ = 1000 μm) under different sinusoidal waveforms and a constant frequency of 0.01 Hz.

Open Access Article. Published on 13 May 2025. Downloaded on 3/6/2026 3:41:36 AM.
This article is licensed under a Creative Commons Attribution 3.0 Unported Licence.

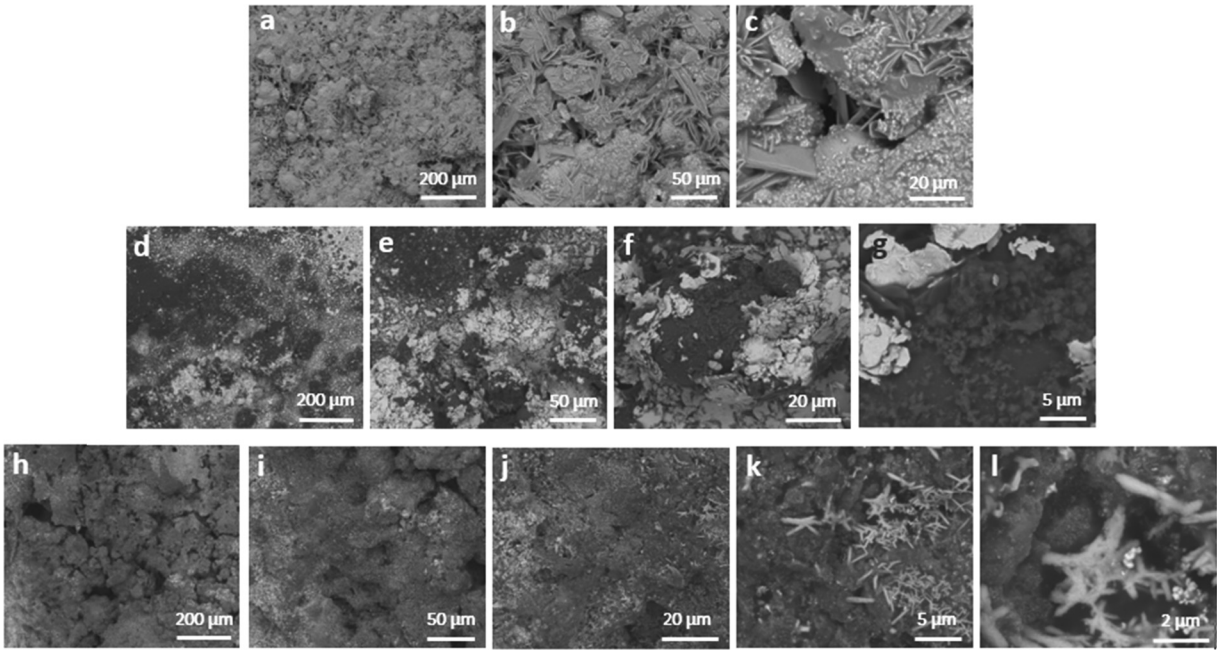

Fig. 6 (a)–(c) SEM images of IL-functionalized geopolymer samples without silver adhesive to show the natural interaction between the geopolymer and $EMIM^+$ Otf^-; (d)–(g) SEM images of IL-functionalized geopolymer samples including a layer of silver adhesive on them before testing; and (h)–(l) SEM images of IL-functionalized geopolymer samples after testing. (ϕ = 1000 μm and h = 140 μm for all the samples).

structures are observed after testing, further magnified in Fig. 6l. Although these regions suggest compositional changes, their exact nature cannot be determined through SEM alone; thus, the morphological structure were further investigated using EDX elemental mapping as presented in Fig. 7.

EDX analysis was performed to confirm the presence and distribution of key elements across various regions of the IL-functionalized GP samples. Fig. 7a shows the EDX spectrum of the GP, highlighting characteristic peaks for Na, Al, and Si, which are attributed to the GP. Additionally, the presence of N, F, and S peaks is attributed to the $EMIM^+$ Otf^-.[22] After electrical stimulation, the EDX spectrum in Fig. 7b reveals the appearance of distinct Ag peaks, particularly in areas 1, 2, and 5 accompanied by oxygen peaks. These observations confirm localized silver oxidation, corresponding to the crystal-like structures observed in the SEM image of Fig. 7b. The silver oxidation process is driven by redox reactions at the electrode–geopolymer interface, initiated under the applied electric potential during testing. The applied voltage facilitates the release of Ag^+ ions from the silver electrode, which subsequently interact with oxygen to form Ag_2O.

In electrochemical metallization (ECM) type memristors, redox reactions at the electrode–electrolyte interface play a crucial role in forming and breaking conductive filaments, thereby enabling memristive properties.[61] However, geopolymer memristors exhibit a different mechanism, involving electroosmosis-based bulk memristive behavior.[19,20] The use of silver electrodes in geopolymer devices has been shown to involve redox reactions of silver ions, as evidenced by the observed silver oxidation in EDX analysis. This necessitates further investigation into how these redox reactions impact the device's memristive performance. One of the most reliable methods to investigate the nature of the redox reactions at the electrode–electrolyte interface is CV. Previous studies on the ECM-type memristors have demonstrated that CV characterizations can reveal the redox reactions associated with the formation and breaking of conductive filaments.[62,63] Peaks in the CV plot typically correspond to these redox reactions and can be compared against the CV profiles of standard reference electrodes for validation. The CV experiment, however, cannot be conducted at the programming voltage corresponding to memristive switching, since that would not reveal the resistive switching behavior and thus the redox reaction peaks would not be captured on the CV characteristic curve.[63]

In the CV experiments carried out in this study, three different sizes (5 samples of size 200 μm, 5 samples of size 500 μm, and 5 samples of size 1000 μm) of micron-scale GP memristors were selected, including both IL-functionalized and pristine GP samples. Prior to the CV tests, each sample underwent I–V sweeps to determine the voltage at which they demonstrate pinched hysteresis in I–V plot. Subsequently, a lower voltage (for which hysteresis pinched I–V plot is not observed) was selected for the CV measurements. For the pristine GP memristors, samples were fully dehydrated at ambient conditions and in the oven for a week to assure water evaporation from the material pores. Fig. 8a and b demonstrate the I–V (at left) and CV plots (at right) for both the pristine and IL-functionalized GP memristors, respectively. As shown in Fig. 8a, the pristine GP memristors did not show pinched hysteresis at 10 V and at 5 V (insets in orange in each CV plot). The absence of pinched hysteresis indicates that they did not exhibit any memristive properties. This is because they were allowed to lose

 This journal is © The Royal Society of Chemistry 2025

Open Access Article. Published on 13 May 2025. Downloaded on 3/6/2026 3:41:36 AM.
This article is licensed under a Creative Commons Attribution 3.0 Unported Licence.

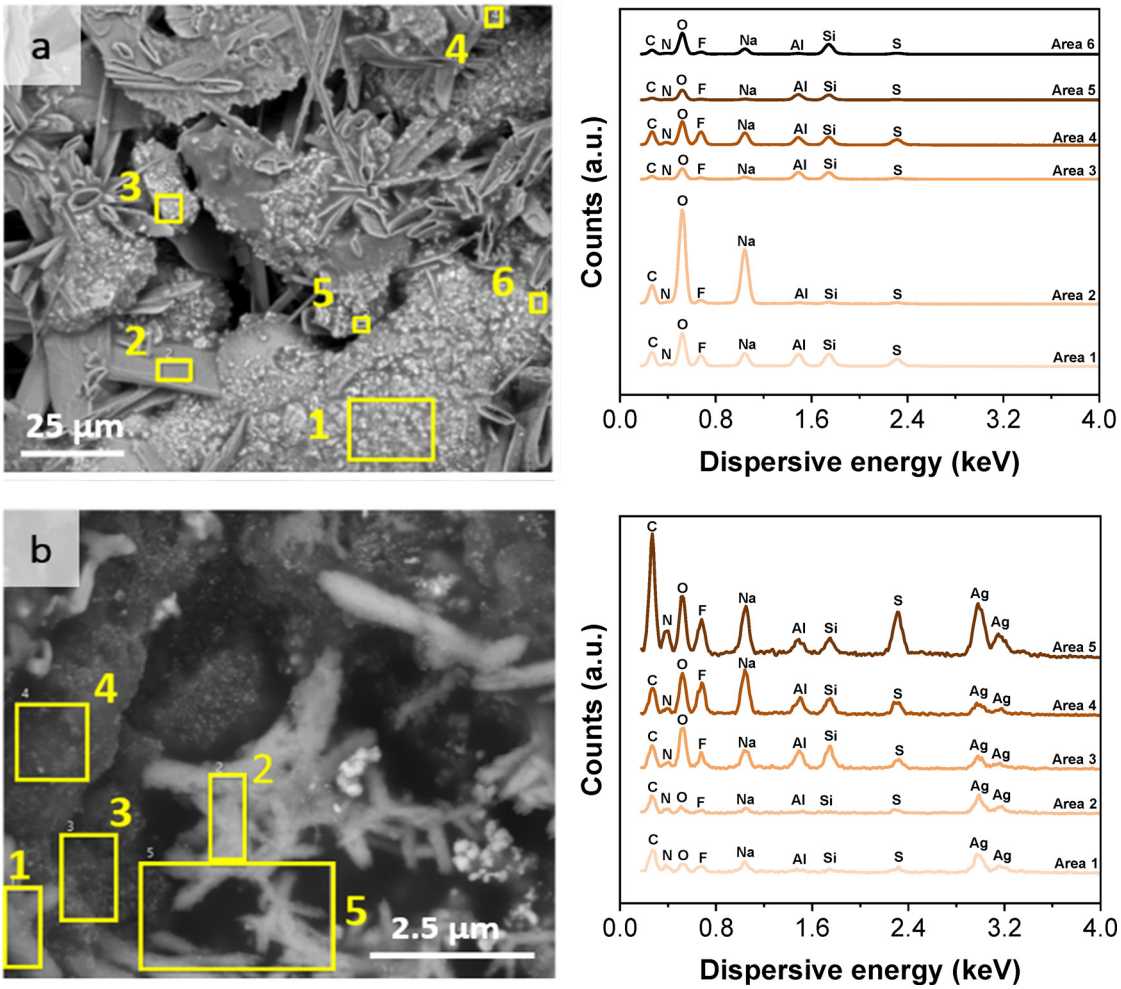

Fig. 7 EDX spectra of the IL-functionalized geopolymer (a) without silver adhesive applied, and (b) after testing.

moisture content, fully dehydrating the pores and capillaries. This also validates our proposed electroosmosis-based model on the memristive properties of geopolymers that hydration of the pores is essential for them to exhibit memory properties.[19,20] The CV plots in Fig. 8a show peaks at +1.8 V and −2.1 V (200 μm sample) +1.65 V and −1.6 V (500 μm and 1000 μm samples), which are very close to the standard potentials of redox reactions of Ag in aqueous solutions (0.8 V and 1.98 V).[64] Previous studies on ECM memristors with Ag electrodes attribute similar peak voltages to Ag oxidation–reduction processes.[63] It is observed that no additional peaks are present in the CV plot up to the applied voltage of 5 V. Further tests at varying scan rates ranging from 1 mV s^{-1} to 500 mV s^{-1} yielded consistent peak shifts between 1.65 V and 2.2 V, similar to prior findings[62,63] (Fig. S14, ESI†).

As shown in Fig. 8b, the *I–V* plots of the IL-functionalized GP memristors reveal the characteristic pinched hysteresis loop when tested in ±10 V range, this behavior was not observed when tested in the lower voltage range of ±5 V. Complementary *I–V* tests conducted at 5 V similarly showed an absence of pinched hysteresis (insets in orange in each CV plot). This observation is attributed to the aging of the IL-functionalized samples for more than a month, which leads to reduced ionic mobility due to the redistribution or partial immobilization of ions within the geopolymer matrix. Structural changes such as densification could further limit ion migration pathways, while the redistribution of the IL over time may result in localized depletion and non-uniform ionic conduction. These combined effects likely diminish the electrochemical dynamics required for memristive behavior, particularly at lower voltages. CV plots in Fig. 8b show a current peak at −1.4 V for the 200 μm sample, subtle peaks at +2 V, +1 V, −0.8 and −2.8 V for the 500 μm sample, and at +2.05 V and −2 V for the 1000 μm sample. These peaks can be attributed to the oxidation and reduction of Ag also in IL-functionalized GP samples. Further scans across different scan rates verified similar trends (Fig. S14, ESI†).

It is established that larger electrode contact areas in memristors can impair their resistive switching performance due to the diminished electric field-enhanced drift-diffusion of Ag^{+} ions.[65] Additionally, larger electrode surfaces lead to high programming currents and necessitate greater voltage to achieve memristive switching.[66,67] In the current study, the ϕ/h ratios of GP devices range from 1.43 : 1 to 7.14 : 1. Such high ϕ/h ratios suggests that electrochemical interplay at the Ag electrode–electrolyte interface may not contribute significantly to

Open Access Article. Published on 13 May 2025. Downloaded on 3/6/2026 3:41:36 AM.
This article is licensed under a Creative Commons Attribution 3.0 Unported Licence.

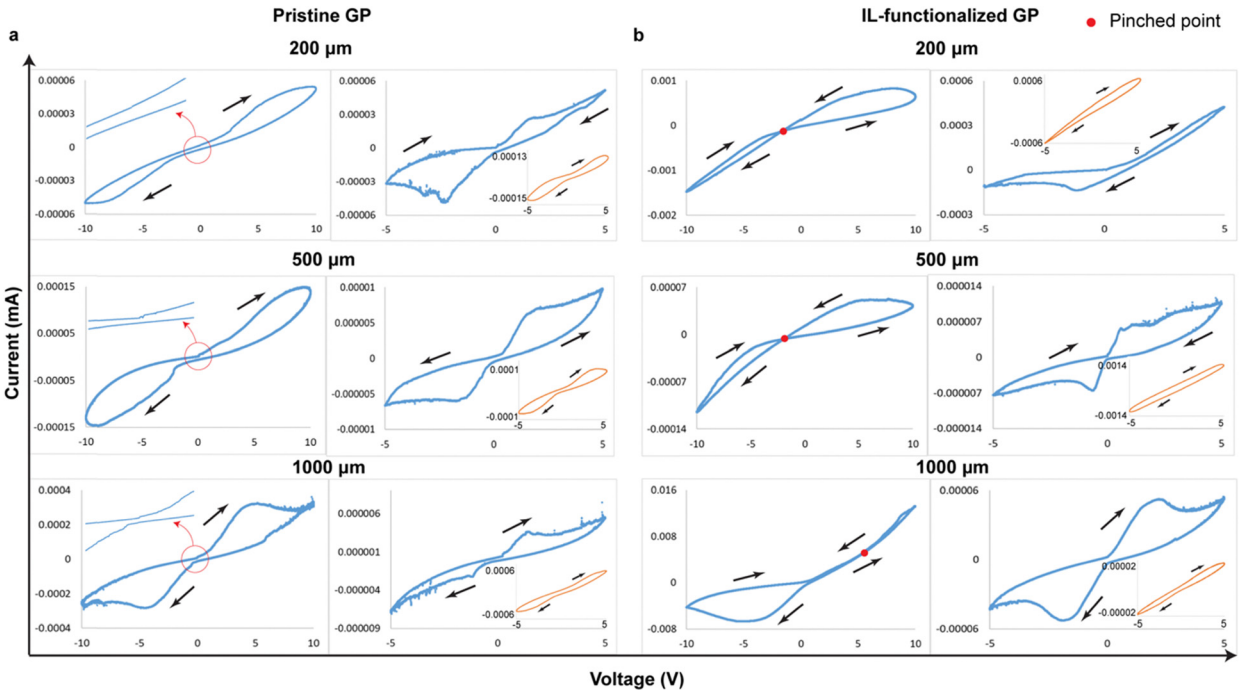

Fig. 8 (a) I–V (left) and CV (right) plots of pristine GP memristors of sizes 200 µm, 500 µm, and 1000 µm. The voltage sweeps were conducted at 5 V, and no pinched hysteresis was observed. The CV tests were conducted at 1 mV s^{-1} rate for the sample of size 200 µm and at 5 mV s^{-1} rate for samples of sizes 500 µm and 1000 µm, showing peaks at +1.8 V and −2.1 V (200 µm sample) +1.65 V and −1.6 V (500 µm and 1000 µm samples). These values are close to the oxidation and reduction potential of Ag in aqueous solution. The insets in orange in each CV plot demonstrate the I–V plot of the corresponding sample at the sample amplitude, without any pinched hysteresis; (b) I–V (left) and CV (right) plots of IL-functionalized GP memristors of sizes 200 µm, 500 µm, and 1000 µm. A voltage sweep conducted at 10 V showed pinched hysteresis. At lower voltages, no pinched hysteresis was observed. CV plots of the IL-functionalized samples, conducted at 5 V and scan rates of 5 mV s^{-1} for the sample of sizes 200 µm 500 µm, and at 50 mV s^{-1} for samples of sizes and 1000 µm. A current peak at −1.4 V is observed for the 200 µm sample, subtle peaks at +2 V and −2.8 V for the 500 µm sample, and clear subtle peaks at +2.05 V and −2 V for the 1000 µm sample are observed. These peaks are indicative of redox reactions of Ag. The insets in orange in each CV plot demonstrate the I–V plot of the corresponding sample at the same amplitude without any pinched hysteresis.

the overall conductivity of the GP memristors. Notably, ECM-type memristors typically feature much smaller surface-to-thickness ratios, where redox reactions substantially influence the formation of conductive filaments. However, in micron-scale devices with high ϕ/h ratios, the larger electrode surface compared to the thickness reduces the likelihood of forming conductive filaments through electrochemical interactions at the electrode–electrolyte interface. This conclusion is supported by the I–V and CV results shown in Fig. 8, which indicate that the redox reaction at the interface does not contribute sufficiently to induce memristive behavior in either pristine or IL-functionalized GP samples.

Based on these comprehensive analyses, it can be inferred that while there are clear indications of redox reactions at the outer surface of both types of GP samples, there is no evidence to suggest that these reactions contribute to the formation of conductive filaments that could induce memristive properties. Despite the presence of voltage peaks in the CV plots for both dehydrated pristine and IL-functionalized samples, no pinched hysteresis was observed in the I–V plots at comparable voltage sweeps, reinforcing the conclusion that silver oxidation does not play a role in the memristive mechanism of geopolymer devices.

Spectroscopy tests on the pore solution of the pristine geopolymer memristors revealed that the pore solution contains Na^+ ions that contribute to the change in the conductivity of the pores, leading to the observed memristive properties of the device. Inductively coupled plasma–mass spectroscopy (ICP–MS) test results in Table 2 show that the concentration of Na^+ ions is the highest in comparison to the negligible concentrations of Mg^{2+} and Fe^{3+} ions. These tests further validate that Na^+ ion channels represent the major contribution to the observed switching mechanism in the pristine geopolymer memristors and that silver ions are not present in the pore solution.

Resistive switching

The ability to achieve stable and reliable resistive switching behavior in memristive devices is crucial for both memory storage and neuromorphic computing applications.[68,69] In the biological context, synapses in the brain adapt and store information by modulating their electrical resistance in response to incoming stimuli, a phenomenon essential for learning and memory retention. Mimicking this synaptic plasticity through resistive switching in memristors is a key objective in developing brain-inspired computing systems. In this study, the endurance and retention performance of GP devices were examined to ensure their long-term functionality, a critical requirement for real-world applications such as energy-efficient

Open Access Article. Published on 13 May 2025. Downloaded on 3/6/2026 3:41:36 AM.
This article is licensed under a Creative Commons Attribution 3.0 Unported Licence.

Table 2 ICP-MS results of pristine GP memristors

	Concentration (Parts Per Billion)					
Element	Na^+ [no gas]	Na^+ [He]	Mg^{2+} [no gas]	Mg^{2+} [He]	Fe^{3+} [no gas]	Fe^{3+} [He]
Sample 1	76332.04	56426.9	354.682	235.986	367.12	275.012
Sample 2	72870.3	57573.38	486.227	340.349	278.146	199.633
Average	74601.17	57000.14	420.4545	288.1675	322.633	237.3225

memory devices and in-memory computing architectures.[69] The endurance performance of the micron-scale IL-functionalized GP memristors is demonstrated in Fig. 9. To ensure the robustness and reliability of the measurement method for resistive switching behavior, we adopted the pulsed method for retention recommended previously.[5,70,71] As shown in Fig. 9a, a complete switching cycle starts with a write pulse of amplitude 0.5 V, followed by a read pulse (0.1 V, 20 ms). Afterward, an erase pulse of amplitude −0.5 V followed by a read pulse (0.1 V, 20 ms) completed the switching cycle. As such, the change in the conductance states was ideally tracked by applying a sequence of read, write, read, and erase pulsed voltage stresses (PVS), facilitating the simultaneous measurement of the output current. The typical resulting plot is used to confirm the presence of resistive switching by observing the set and reset transitions and comparing the average values of high-resistance state (HRS) and low-resistance state (LRS) during the read pulses. In Fig. 9b, IL-functionalized GP memristors show stable HRS and LRS beyond 20 000 cycles using a read voltage of only 0.1 V. Comparing with our previous work on bigger GP memristors of thickness 11 mm and requiring 5 V,[20] the low programing voltage can be attributed to the smaller dimension of the devices. The retention performance of GP memristors is better than many previous studies, where only less than 5000 cycles were achieved.[72–81] For instance, Zhao *et al.*[75] developed a biocompatible Chitosan-reduced Graphene Oxide (CS-rGO) memristor with an interpenetrating network electrolyte structure that demonstrated stable bipolar resistive switching over just 100 cycles. Similarly, Feng *et al.*[78] reported a memristor based on oxidized $Ti_3C_2T_x$ MXene that exhibited excellent bipolar resistance switching properties with a cyclic endurance of over 1000 cycles. Despite this performance, the endurance remains limited compared to the IL-functionalized GP memristors, highlighting the enhanced robustness and longevity of our micron-scale GP devices, making them more suitable for long-term applications in memory storage and neuromorphic computing systems.

The resistance switching characteristics can be observed in Fig. 9b, where the resistance HRS and LRS values are uniformly distributed. It is evident that the first few cycles show a drastic drop in the HRS value, which immediately stabilizes and continues for the entirety of the retention cycles. The dynamics of ionic transport inside the GP memristors could be responsible for this initial drop in HRS values. As the Na^+ ions start moving under the effect of external electric stimuli, the number of ions initially available in the diffuse layer of the electric double layer is low, which results in very high resistance of the device. As the switching cycles repeat a few times, more ions from the Helmholtz layer get liberated into the diffuse layer, increasing the device's conductivity. As a result, the HRS state keeps dropping drastically. Once the maximum number of Na^+ ions are available in the diffuse layer, the HRS value sets to a stable state and continues for the rest of the retention cycles.

Synaptic properties

In biological synapses, the ability to retain memory and dynamically adapt to electrical stimuli is critical for learning and

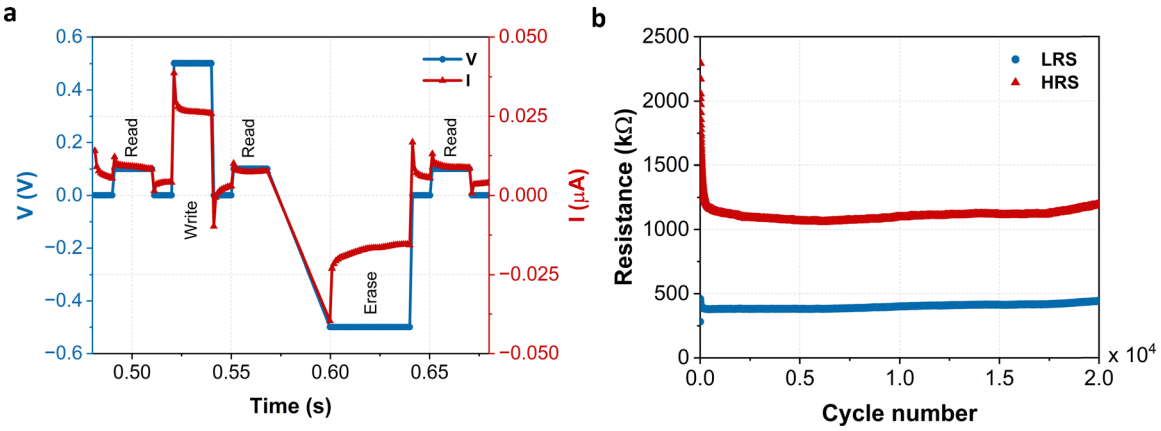

Fig. 9 Resistive switching properties; (a) measurement of change in conductance state during a resistive switching cycle in an IL-functionalized GP memristor. There is a read pulse of 0.1 V, 20 ms between the write pulse (0.5 V, 20 ms) and the erase pulse (−0.5 V, 50 ms) which completes a full acquisition; (b) the cycle in a was repeated over 20 000 times demonstrating retention window of IL-functionalized GP memristors over 20 000 cycles with reading voltage of 100 mV.

Open Access Article. Published on 13 May 2025. Downloaded on 3/6/2026 3:41:36 AM.
This article is licensed under a Creative Commons Attribution 3.0 Unported Licence.

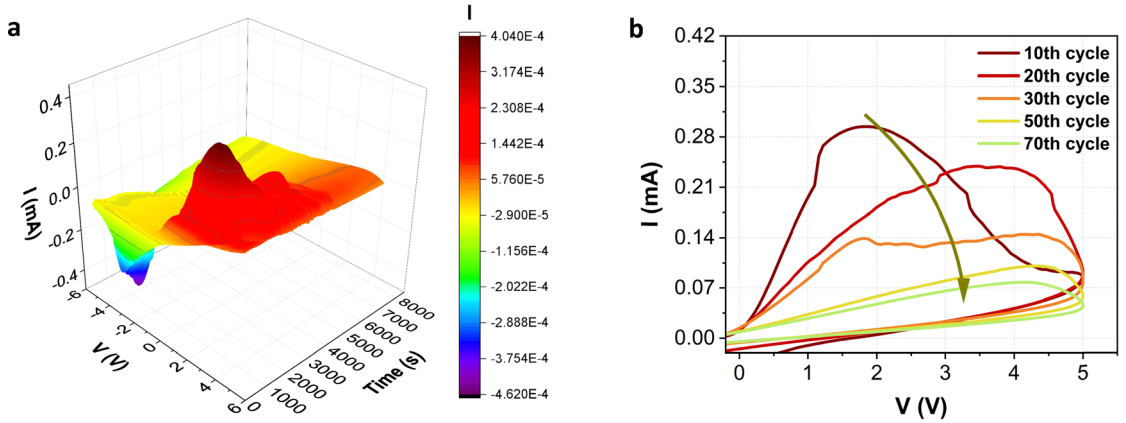

Fig. 10 (a) 3D surface plot showing the evolution of the pinched hysteresis loop in a micron-scale IL-functionalized GP over 2 hours; (b) a cross-sectional view of the hysteresis plot's evolution over 70 cycles.

long-term stability. To investigate these properties in the sub-millimeter scale IL-functionalized geopolymer device, the evolution of its pinched hysteresis loop over time is studied (Fig. 10).[22] This migration results in dynamic charge storage and release, effectively mimicking the adaptive plasticity of biological synapses, where synaptic strength is modulated by both the duration and frequency of stimuli—a behavior that was explored in previous experiments (see Fig. 2). The 2D cross-sectional view in Fig. 10b further illustrates the changes in the hysteresis loop over successive cycles. Initially, the device exhibits strong charge trapping and significant ion migration, resulting in broader hysteresis loops. Over time, however, the system undergoes ionic relaxation, leading to a gradual narrowing of the loop as the device reaches electrochemical equilibrium. This shift in synaptic weight, as the sweeping was repeated for 70 cycles—mirroring the depression observed in biological synapses—also reflects the behavior of synapses adapting to repeated stimuli, where a steady conductive state is achieved after continuous electrical input.[19,20,82]

In biological systems, a synapse is the point where neurons connect to communicate using electrical or chemical signals.[70] Biological synapses adapt to external stimuli through synaptic plasticity, a process that modifies their strength based on activity, enabling the storage and processing of information.[71] The micron-scale memristive GP devices studied here function in a way that mirrors the operation of biological synapses, both in design and activity (see Fig. 11a). A natural synapse links two neurons, termed upstream (pre-synaptic) and downstream (post-synaptic) neurons, according to the neurotransmitter movement. These components are crucial for generating impulses that either activate (excite) or suppress (inhibit) the synapse. When exposed to continuous activating signals, the synapse strengthens, while suppressive signals cause it to weaken. This adaptation, seen in biological systems, is replicated in artificial synapses, which can similarly increase (potentiation) or decrease (depression) in strength.

Synaptic plasticity properties can be assessed in artificial synapses by applying consecutive voltage sweeps.[5,83–86] As such, 15 IL-functionalized GP memristors were tested to evaluate their synaptic behavior. As shown in Fig. 10b, consecutive positive voltage sweeps induce a shift in the positive loop of the *I–V* characteristic plot up to the 70th cycle. However, this method is only an initial experimentation to test synaptic plasticity properties in memristors. To simulate the synaptic plasticity learning rule in artificial synapses, one must first examine the resistance or conductance gradient adjustment and identify appropriate excitatory and inhibitory pulse stimulations, as demonstrated in previous studies.[20,55,87,88] These stimulations ensure the device's weight adjustment is stable and repeatable. Excitatory pulse stimulation enhances synaptic connection strength and increases synaptic weight, resulting in increased conductance and decreased resistance. Conversely, inhibitory pulse stimulation reduces synaptic weight, thereby decreasing conductance and increasing resistance.

In this study, we utilized the GP device as a synaptic model and varied the amplitude and pulse width for repeated tests. Fig. 11b shows the definition of different pulse parameters used in this study. It was observed that the positive pulse lowered the device's current, serving as an inhibitory pulse, while the negative pulse raised it, acting as an excitatory pulse, as shown in Fig. 11a. To test the retention of synaptic plasticity properties of our devices, we repeated the cycles of potentiation and depression for an indefinite time and found that they showed stable retention for up to 4000 cycles (Fig. 11d). Each cycle consists of 100 steps of potentiation pulse followed by 100 steps of depression pulse. Thus, the devices demonstrate a robust retention property for 800 000 pulses.

Adjusting various pulse parameters allowed for the expected synaptic weight modulation. As shown in Fig. S15 (ESI†), within the same range of current change, increasing the pulse height from 100 mV to 500 mV, the potentiation trend changed to depression trend of synaptic weight adjustment. This is attributed to the fact that a shorter pulse width equates to smaller pulse energy, necessitating fewer pulses for electroosmotic flow to traverse the pores vertically. Consequently, to achieve more consistent and accurate synaptic weight control, we tailored the parameters of both excitatory and inhibitory pulses. As presented in Fig. S16 (ESI†), the optimal synaptic weight modulation is

Open Access Article. Published on 13 May 2025. Downloaded on 3/6/2026 3:41:36 AM.
This article is licensed under a Creative Commons Attribution 3.0 Unported Licence.

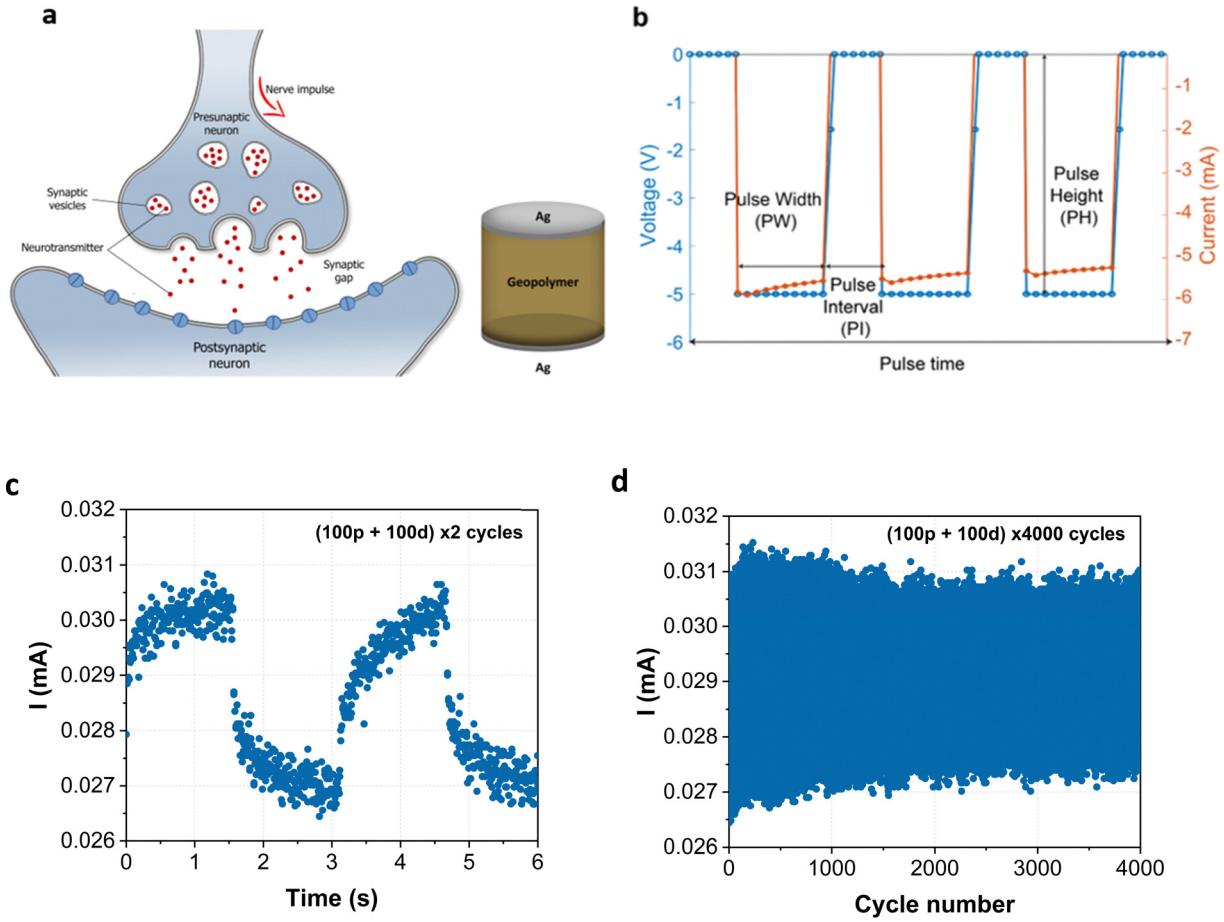

Fig. 11 (a) Structural and functional similarities of IL-functionalized GP memristor with a biological synapse. The geopolymer material works as the synapse, where the top and bottom silver electrodes function as the pre-synaptic and post-synaptic sites of a biological synapse; (b) schematic of pulsed voltage used in demonstrating synaptic behavior, showing pulse parameters: pulse width (PW), pulse interval (PI), and pulse height/amplitude (PH); (c) response of GP device synaptic weights under stimuli with inhibitory and excitatory pulses with reproducible behavior of synaptic weight modulation demonstrating synaptic potentiation and depression. The cycle has been repeated two times. Each cycle contains 100 potentiation pulses followed by 100 depression pulses; and (d) retention characteristics of IL-functionalized GP artificial synapses demonstrating repeatability of potentiation–depression cycle shown in c for 4000 cycles.

achieved with a pulse interval of 1–10 ms, a fixed pulse width of 20 ms, and a pulse amplitude of 500 mV. Additionally, Fig. S17 (ESI†) demonstrates the behavior of the device across varying pulse widths at a constant pulse amplitude of 500 mV and a pulse interval of 5 ms. Among the tested pulse widths, 20 ms provided the most stable output, reinforcing its suitability as an artificial synapse. These parameters enable precise and uniform adjustment of the device's resistance within a defined range, facilitating further characterization of its synaptic properties.

When synaptic plasticity is governed by the frequency of excitation, it is called spike-frequency-dependent-plasticity (SRDP). SRDP is an important information-processing method for biological synapses. In this method, neuronal information transfer is encoded in firing frequency rather than temporal relationships.[89–91] When post-synaptic neuron activity remains at a extremely low frequency, it will not cause synaptic regulation. This frequency can be considered that neurons are uniformly in a resting state. LTD and LTP are induced when post-synaptic neuron activities occur at higher frequencies.[3,92]

SRDP depends on the number and intervals of pulses applied.[89,93,94] To observe this behavior in GP memristors, P-spike groups with different pulse numbers and intervals were applied to the device while variations in synaptic weight were monitored (Fig. 12a). P-Spikes are the spiking voltage pulses that induce potentiation in the device. When the P-spike had a longer interval (500 ms), the current (synaptic weight) change did not increase with increasing number of spikes. However, the change in current increased with the increasing number of spikes when the spike interval decreased. In particular, the current change increased considerably as the number of spikes increased at a short spike interval (5 ms). Therefore, the synaptic weight change of the GP memristor was affected by the spike number and interval.

When a pair of pre-synaptic pulses enhance or inhibit the second post-synaptic response, it is called paired-pulse facilitation-PPF (when enhanced) or depression-PPD (when inhibited).[95,96] A longer duration of PPF is called post-tetanic potentiation (PTP).[20,71] An artificial synapse can demonstrate

Open Access Article. Published on 13 May 2025. Downloaded on 3/6/2026 3:41:36 AM.
This article is licensed under a Creative Commons Attribution 3.0 Unported Licence.

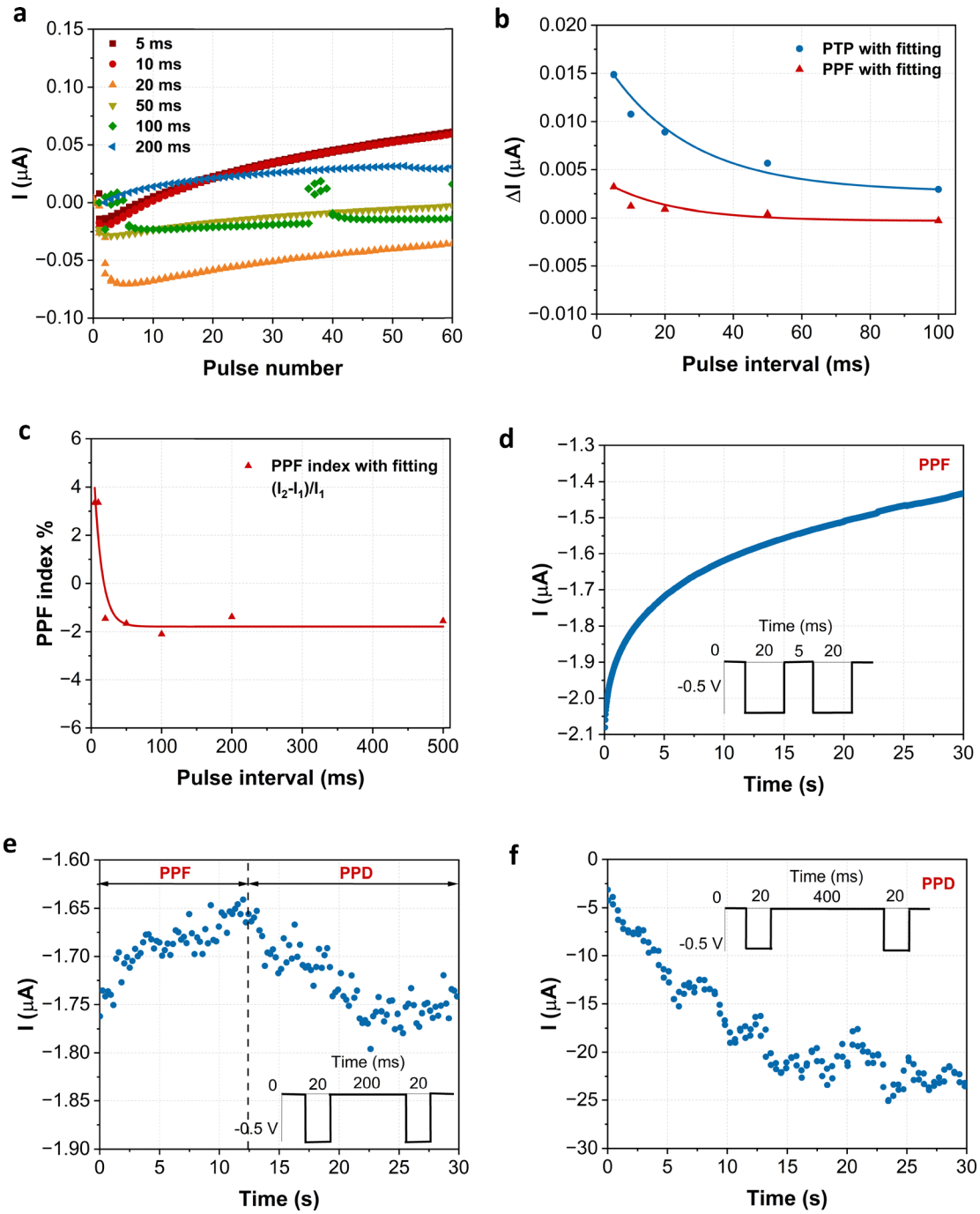

Fig. 12 (a) Variation of ΔI in terms of P-spike pulse number obtained at different P-spike rates (pulse amplitude of −0.5 V and width of 20 ms). Similar trends were observed across 7 devices of varying diameters. Representative data from one device of diameter 1000 μm are shown here; (b) variations of $(I_2 - I_1)$ and $(I_{10} - I_1)$ with respect to the P-spike interval, corresponding to the PPF and PTP of the biological synapse, respectively. Data were fitted using the equation PPF/PTP = $C_1e^{-t/\tau 1} + C_2e^{-t/\tau 2} + C_3$. For PPF, C_1 = 0.00226, τ_1 = 18.033, C_2 = 0.00226, τ_2 = 22.040, C_3 = −2.980 × 10^{-04}. For PTP, C_1 = 0.00746, τ_1 = 22.401, C_2 = 0.00746, τ_2 = 27.379, C_3 = 0.00268; (c) PPF index plot fitted using an exponential model, where PPF index = $C_1e^{-t/\tau 1} + C_2e^{-t/\tau 2} + C_3$. Here, C_1 = 2.775, τ_1 = 36.1809, C_2 = 2.775, τ_2 = 44.22, C_3 = −1.9. Twenty devices (1000 μm diameter) were tested for PPF, PTP, and PPF index characterization. The curves were fitted using seven data points per device; (d) demonstration of PPF. The pulse interval was tuned to 5 ms to achieve this facilitation. Other pulse parameters are PH: −0.5 V, PW: 20 ms; (e) both PPF and PPD occurs when the pulse interval increases to 200 ms. Other pulse parameters are the same as in d; (f) only PPD occurs when the pulse interval further increases to 400 ms. Other pulse parameters are the same as in d.

these types of SRDP, given that a pair of post-synaptic current (PSC) is generated for a pair of input voltage pulses. When the output current is excitatory post-synaptic current (EPSC), it will induce PPF. Conversely, when the output current is inhibitory

Open Access Article. Published on 13 May 2025. Downloaded on 3/6/2026 3:41:36 AM. This article is licensed under a Creative Commons Attribution 3.0 Unported Licence.

post-synaptic current (IPSC), it will induce PPD synaptic mimic. IL-functionalized GP memristors demonstrate PPF, PPD, and PTP behavior, which are demonstrated in Fig. 12b–f.

The dependence of the synaptic weight on the spike rate (or interval) is clearly indicated in Fig. 12b with the demonstration of PPF and PTP, where the difference between the first current (I_1) and nth current (I_N), $\Delta I = I_N - I_1$, is shown in terms of number of spikes obtained at various spike rates. Fig. S18 (ESI†) shows a schematic of a typical pair of pulses used in this study. The application of P-spikes with shorter intervals induces a greater change in conductance. We can observe that change in the output current (ΔI) is decreasing with an increase in the pulse interval, as observed for other memristors.[97,98] This phenomenon can be ascribed to the nature of the memristive properties observed in GP. In our previous work,[19] we showed that the time-dependent conductance change in GP is related to the electroosmosis-induced ion channels inside the material pores. When an electric field is applied, the water inside the pores moves by dragging along Na^+ ions and locally changing the conductance of the material. This phenomenon is dependent upon the rate of stimuli. If the input voltage pulses are applied at a longer interval, the water moves slowly inside the material pores, and it starts coming back before significantly changing the filling of the pores, resulting in a conductance change and consequently increasing the output current.

The change in current within consecutive pairs of pulses is termed the PPF index,[96] which can be measured as $(I_2 - I_1)/I_1$. Fig. 12c demonstrates the PPF index of our devices, where it begins at 1.4% and exponentially reduces to zero and further to the negative value. This behavior can be related to the SRDP demonstrated in Fig. 12a. Due to the nature of the pairs of pulses, the PPF index gradually reduces, instead of the opposite trend we observed in our previous study for the bigger sized GP memristors.[20] As demonstrated in this study, positive voltage pulses are excitatory for the IL-functionalized GP memristors, which creates this trend in the PPF index. The initial negative ΔI observed in Fig. 12b and c reflects a transient reduction in current during the first few pulses, which transitions to positive values after approximately seven pulses. This behavior is consistent with the device's dynamic response to consecutive stimuli, where the system undergoes an initial adjustment phase before stabilizing. For PPF and PTP, individual device outputs from three representative devices and their averaged data points with error bars representing variability across multiple devices have been presented in Fig. S19 (PPF) and S20 (PTP) (ESI†), showing similar trend as in Fig. 12b. For PPF index, individual device outputs from another three representative devices and the averaged data points for all four devices with error bars representing variability across multiple devices have been presented in Fig. S21 (ESI†) showing similar trend as in Fig. 12c. A similar trend in the PPF index can be observed in previous studies.[68,99–103]

It was further observed that the devices showed paired-pulse facilitation (PPF) phenomenon for pulse intervals shorter than 200 ms. Fig. 12d demonstrates that a pulse interval of 5 ms induced only PPF behavior. When the pulse interval equals 200 ms, the devices exhibit PPF followed by PPD after 20 s (Fig. 12e). Similar behavior was observed in previous studies.[20,104] For pulse intervals longer than 400 ms, GP memristors exhibit only depression, emulating a PPD,[105–107] as shown in Fig. 12f. This observed depression for an intermediate pulse interval of 200 ms might be due to the interplay between the dynamics of Na^+ ion channels.

The relative timing between the pre-synaptic and post-synaptic spikes can greatly affect the nature of long-term synaptic modification,[106,107] the study of which is called the Hebbian learning rule.[108,109] When the timing of pre- and post-synaptic spikes is precisely controlled, the artificial synapses can mimic the long-term memory properties of a biological synapse, a phenomenon known as spike-timing-dependent-plasticity (STDP). To demonstrate STDP behavior in an artificial synapse, the two terminals of the device are usually considered as pre-synaptic and post-synaptic sites for stimulation. The polarity and relative time difference ($\Delta t = t_{post} - t_{pre}$) between the pre-synaptic spike and the post-synaptic spike is then precisely controlled. The top and bottom electrodes were stimulated using precisely controlled pairs of spiking voltage pulses, and they were considered to be pre-synaptic and post-synaptic sites, respectively, as shown in Fig. S2 (ESI†). A relative time difference Δt, was maintained between the pre-spike and post-spike pulses. When the spike was applied to the top prior to the bottom electrode, Δt was positive. When the spike was applied to the bottom prior to the top electrode, Δt was negative.

Fig. 13a represents Asymmetric Hebbian learning implemented in IL-functionalized GP artificial synapses. Pairs of pre-spike and post-spike with intervals ranging from 40 ms to 240 ms were utilized to stimulate the GP. The change in conductance was recorded simultaneously after applying the pulses. It can be observed that ΔW decreases when Δt increases along with both polarities. It is also observed that some of the IL-functionalized samples showed deviation in their STDP behavior, as reflected in their standard deviation values. Future studies are required to probe the contributing factors in such statistical outcomes. Fig. 13b is an example of input voltage applied during STDP characterization: V_{pre} is applied to the top electrode *via* channel 1, and V_{post} is applied to the bottom electrode *via* channel 2 when Δt is greater than 0. Similarly, when Δt is smaller than 0, adjusting the time and the sequence of the pulse parameter can give the right pulse train with precise reading values before and after the pulse is applied, as shown in Fig. 13c. The asymmetric Hebbian/anti-Hebbian learning can be fitted with the following exponential function:

$$\Delta W = C + Ae^{-\Delta t/\tau} \quad (1)$$

where A and τ represent the scaling factor and time constant of the exponential function, respectively. It is important to note that eqn (1) fits both asymmetric Hebbian and asymmetric anti-Hebbian, depending on the sign of the fitting parameters. Studies suggest the value of ΔW in these Hebbian learning rules depends not only on the shape and time delay between the pulses but also on the initial value of the output current.[20,68]

Open Access Article. Published on 13 May 2025. Downloaded on 3/6/2026 3:41:36 AM.
This article is licensed under a Creative Commons Attribution 3.0 Unported Licence.

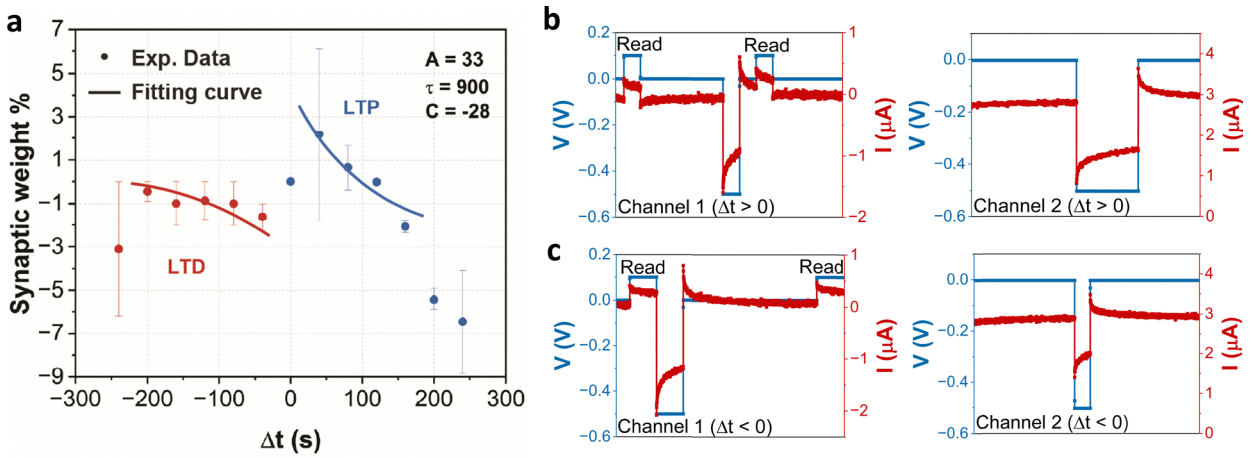

Fig. 13 (a) Asymmetric Hebbian learning classic spike-time dependent plasticity plot occurs from the time range of 0–150 ms; (b) pulse-current result from 2 different channels, indicating pre and post synaptic stimuli when the delta *t* is greater than 0; (c) shows the pulse-current result from 2 different channels, indicating pre and post synaptic stimuli when the delta *t* is less than 0.

These observations demonstrate that stable Hebbian learning is generated from STDP in the biological brain.[110] When mimicked in artificial synapses, they can facilitate self-adaptation.[111]

Conclusions

In this work, geopolymer memristors were successfully manufactured at micron scales as small as 200 μm, achieving a substantial volume reduction of 61.6 × 10^3 times compared to previous designs. However, this reduction in size resulted in faster degradation of memristive properties, with 90% of micron-sized pristine geopolymer devices losing their memristive behavior in less than a week. The addition of $EMIM^+$ Otf^- played a crucial role in overcoming this limitation by significantly enhancing the device longevity for more than three weeks. This improvement is attributed to the replacement of water within the porous geopolymer structure with IL, which stabilizes ionic pathways, prevents structural degradation, and mitigates the effects of water evaporation during aging. The size reduction and IL functionalization enabled operation at significantly lower activation voltages, with IL-functionalized micron-scale devices achieving a minimum activation voltage of 0.3 V, compared to the 5 V activation voltage required for cm-scale devices, highlighting their potential for low-power applications. Furthermore, these IL-functionalized devices exhibit the characteristic fingerprints of memristors, demonstrating stable resistive switching behavior for over 20 000 cycles with minimal read voltage. In addition, IL-functionalized geopolymer memristors exhibit various synaptic plasticity behaviors, such as potentiation–depression, paired-pulse facilitation and depression, post-tetanic potentiation, and Hebbian learning through spike-timing-dependent plasticity. SEM, EDX, and CV analysis confirmed the oxidation of Ag at the electrode–geopolymer interface in both pristine and IL-functionalized devices. However, only the IL-functionalized devices displayed pinched hysteresis in *I–V* plots at the testing conditions, indicating that Ag oxidation did not contribute to memristive behavior. Beyond memristive switching and synaptic behavior, geopolymers exhibit multifunctional properties such as piezo resistivity and piezoelectricity, enabling their use in self-powered sensing and computing platforms. These capabilities position geopolymers as a promising material for intelligent structural health monitoring (SHM), enabling the integration of real-time sensing, adaptive learning, and autonomous damage detection within a single system.

Future research will focus on improving device repeatability by precisely controlling porosity at microscale using cost-effective, natural pore-forming agents. Enhancing structural uniformity could improve device consistency, further unlocking their potential for energy-efficient neuromorphic computing and next-generation smart infrastructure.

Author contributions

M. A. performed geopolymer sample fabrication and conducted material characterization tests including SEM and EDX; M. A. S. and Z. G. performed CV and ICP-MS characterization tests; *I–V* Characterization was conducted by M. A.; Device characterization for memristive switching and synaptic properties were conducted by Z. G. and M. A. S.; M. A. and M. A. S. wrote the manuscript; S. A. S., C. L., and R. M. supervised the research and provided revisions to the manuscript. All authors contributed to the study and approved the final manuscript for submission.

Data availability

All the data supporting the findings of this study, including experimental results, characterization data, *I–V* measurements, *etc.*, are included in the manuscript and ESI.† Due to the experimental nature of this work and its reliance on specialized instruments and proprietary techniques, raw datasets are not

Open Access Article. Published on 13 May 2025. Downloaded on 3/6/2026 3:41:36 AM. This article is licensed under a Creative Commons Attribution 3.0 Unported Licence.

publicly available but can be provided upon reasonable request to the corresponding author.

Conflicts of interest

There are no conflicts to declare.

Acknowledgements

CL acknowledges financial support from the Air Force Office of Scientific Research (grant no FA9550-21-1-0416). RM acknowledges financial support from the U.S. Army Research Office (grant no W911NF-23-2-0020). MA thanks Dr Warren Straszheim, manager of the Materials Analysis and Research Lab at Iowa State University, for his expert guidance in the operation of the scanning electron microscope and energy-dispersive X-ray spectrometry.

References

1 N. A. Goriounova and H. D. Mansvelder, Genes, cells and brain areas of intelligence, *Front. Hum. Neurosci.*, 2019, **13**, 44.
2 A. R. Young, *et al.*, A Review of Spiking Neuromorphic Hardware Communication Systems, *IEEE Access*, 2019, **7**, 135606–135620.
3 Z. Xiao and J. Huang, Energy-Efficient Hybrid Perovskite Memristors and Synaptic Devices, *Adv. Electron. Mater.*, 2016, **2**(7), 1600100.
4 S. E. Thompson and S. Parthasarathy, Moore's law: the future of Si microelectronics, *Mater. Today*, 2006, **9**(6), 20–25.
5 T. Yu, *et al.*, $Hf_{0.5}Zr_{0.5}O_2$-based ferroelectric memristor with multilevel storage potential and artificial synaptic plasticity, *Sci. China Mater.*, 2021, **64**(3), 727–738.
6 A. El Mesoudy, *et al.*, Fully CMOS-compatible passive TiO_2-based memristor crossbars for in-memory computing, *Microelectron. Eng.*, 2022, **255**, 111706.
7 J. Choi, *et al.*, Organic–inorganic hybrid halide perovskites for memories, transistors, and artificial synapses, *Adv. Mater.*, 2018, **30**(42), 1704002.
8 C. Zhang, *et al.*, Recent progress of organic–inorganic hybrid perovskites in RRAM, artificial synapse, and logic operation, *Small Sci.*, 2022, **2**(2), 2100086.
9 J. Xu, *et al.*, Memristors with biomaterials for biorealistic neuromorphic applications, *Small Sci.*, 2022, **2**(10), 2200028.
10 X. Liu, *et al.*, All-Photolithography Fabrication of Ion-Gated Flexible Organic Transistor Array for Multimode Neuromorphic Computing, *Adv. Mater.*, 2024, **36**(21), 2312473.
11 M. Buczek, *et al.*, Large area pulsed laser deposition of memristive $Pr_{0.7}Ca_{0.3}MnO_3$ heterostructures for neuromorphic computing, *Thin Solid Films*, 2024, **805**, 140499.
12 S. S. Kundale, *et al.*, Review of electrochemically synthesized resistive switching devices: memory storage, neuromorphic computing, and sensing applications, *Nanomaterials*, 2023, **13**(12), 1879.
13 L. Chua, If It's Pinched It's a Memristor, in *Handbook of Memristor Networks*, ed. L. Chua, G. C. Sirakoulis and A. Adamatzky, Springer International Publishing, Cham, 2019, pp. 15–88.
14 A. Thomas, Memristor-based neural networks, *J. Phys. D: Appl. Phys.*, 2013, **46**(9), 093001.
15 J. Davidovits, Geopolymers: inorganic polymeric new materials, *J. Therm. Anal. Calorim.*, 1991, **37**(8), 1633–1656.
16 C. Lamuta, *et al.*, Direct piezoelectric effect in geopolymeric mortars, *Mater. Des.*, 2016, **107**, 57–64.
17 S. Candamano, *et al.*, Graphene nanoplatelets in geopolymeric systems: a new dimension of nanocomposites, *Mater. Lett.*, 2019, **236**, 550–553.
18 C. Lamuta, *et al.*, Piezoresistive characterization of graphene/metakaolin based geopolymeric mortar composites, *MRS Adv.*, 2017, **2**(61), 3773–3779.
19 M. A. Shakib, *et al.*, Ion Channels and Electroosmosis in Porous Geopolymers: A Novel Category of Low-Cost Memristors, *Adv. Funct. Mater.*, 2023, **33**(43), 2306535.
20 M. A. Shakib, Z. Gao and C. Lamuta, Synaptic Properties of Geopolymer Memristors: Synaptic Plasticity, Spike-Rate-Dependent Plasticity, and Spike-Timing-Dependent Plasticity, *ACS Appl. Electron. Mater.*, 2023, **5**(9), 4875–4884.
21 H. Sato, *et al.*, Memristors with controllable data volatility by loading metal ion-added ionic liquids, *Front. Nanotechnol.*, 2021, **3**, 660563.
22 Z. Lei, *et al.*, *Introduction: ionic liquids*, ACS Publications, 2017, pp. 6633–6635.
23 Y. Xia, *et al.*, Organic iontronic memristors for artificial synapses and bionic neuromorphic computing, *Nanoscale*, 2024, **16**(4), 1471–1489.
24 H. Yuan, *et al.*, Hydrogenation-Induced Surface Polarity Recognition and Proton Memory Behavior at Protic-Ionic-Liquid/Oxide Electric-Double-Layer Interfaces, *J. Am. Chem. Soc.*, 2010, **132**(19), 6672–6678.
25 P. Bhunia, *et al.*, A non-volatile memory device consisting of graphene oxide covalently functionalized with ionic liquid, *Chem. Commun.*, 2012, **48**(6), 913–915.
26 J. Shi, *et al.*, A correlated nickelate synaptic transistor, *Nat. Commun.*, 2013, **4**(1), 2676.
27 M. Y. Chougale, *et al.*, Memristive switching in ionic liquid–based two-terminal discrete devices, *Ionics*, 2019, **25**(11), 5575–5583.
28 M. U. Khan, *et al.*, Ionic liquid multistate resistive switching characteristics in two terminal soft and flexible discrete channels for neuromorphic computing, *Microsyst. Nanoeng.*, 2022, **8**(1), 56.
29 M. U. Khan, G. Hassan and J. Bae, Soft ionic liquid based resistive memory characteristics in a two terminal discrete polydimethylsiloxane cylindrical microchannel, *J. Mater. Chem. C*, 2020, **8**(38), 13368–13374.
30 M. U. Khan, *et al.*, Soft and flexible: core–shell ionic liquid resistive memory for electronic synapses, *Microsyst. Nanoeng.*, 2021, **7**(1), 78.

Open Access Article. Published on 13 May 2025. Downloaded on 3/6/2026 3:41:36 AM.
This article is licensed under a Creative Commons Attribution 3.0 Unported Licence.

31 Q. Sheng, *et al.*, Transporting an ionic-liquid/water mixture in a conical nanochannel: a nanofluidic memristor, *Chem. Commun.*, 2017, **53**(45), 6125–6127.
32 P. Zhang, *et al.*, Nanochannel-Based Transport in an Interfacial Memristor Can Emulate the Analog Weight Modulation of Synapses, *Nano Lett.*, 2019, **19**(7), 4279–4286.
33 J.-B. Chen, *et al.*, Synaptic Plasticity of a Microfluidic Memristor with a Temporary Memory Function Based on an Ionic Liquid in a Capillary Tube, *J. Phys. Chem. C*, 2023, **127**(6), 3307–3315.
34 T.-T. Guo, *et al.*, Artificial Neural Synapses Based on Microfluidic Memristors Prepared by Capillary Tubes and Ionic Liquid, *J. Phys. Chem. Lett.*, 2024, **15**(9), 2542–2549.
35 Y. Li, *et al.*, Programmable Polymer Memory Device Based on Hydrophilic Polythiophene and Poly(ionic liquid) Electrolyte, *Macromol. Chem. Phys.*, 2015, **216**(1), 113–121.
36 T. Suga, K. Aoki and H. Nishide, Ionic Liquid-Triggered Redox Molecule Placement in Block Copolymer Nanotemplates toward an Organic Resistive Memory, *ACS Macro Lett.*, 2015, **4**(9), 892–896.
37 K. Rajan, *et al.*, Ionic liquid-enhanced soft resistive switching devices, *RSC Adv.*, 2016, **6**(96), 94128–94138.
38 X. Kang, *et al.*, NiO-based resistive memory devices with highly improved uniformity boosted by ionic liquid pretreatment, *Appl. Surf. Sci.*, 2019, **480**, 57–62.
39 B. Sun, *et al.*, A Battery-Like Self-Selecting Biomemristor from Earth-Abundant Natural Biomaterials, *ACS Appl. Bio Mater.*, 2021, **4**(2), 1976–1985.
40 B. Sun, *et al.*, A True Random Number Generator Based on Ionic Liquid Modulated Memristors, *ACS Appl. Electron. Mater.*, 2021, **3**(5), 2380–2388.
41 X. Ye, T. Jin and C. Yun, A review on deep learning-based structural health monitoring of civil infrastructures, *Smart Struct. Syst*, 2019, **24**(5), 567–585.
42 Y. Lee, *et al.*, Structural damage detection using deep learning and FE model updating techniques, *Sci. Rep.*, 2023, **13**(1), 18694.
43 C. R. Farrar and K. Worden, *Structural health monitoring: a machine learning perspective*, John Wiley & Sons, 2012.
44 T.-Y. Wang, *et al.*, Forming-free flexible memristor with multilevel storage for neuromorphic computing by full PVD technique, *J. Mater. Sci. Technol.*, 2021, **60**, 21–26.
45 S.-U. Lee, *et al.*, Artificial Synapse Based on a δ-$FAPbI_3$/Atomic-Layer-Deposited SnO_2 Bilayer Memristor, *Nano Lett.*, 2024, **24**(16), 4869–4876.
46 L. Chen, *et al.*, *ALD Based Flexible Memristive Synapses for Neuromorphic Computing Application. in Electrochemical Society Meeting Abstracts 240*, The Electrochemical Society, Inc, 2021.
47 Y. İ. Keser, K. S. Yıldırım and D. Gökcen. Patterning Titanium Dioxide Based Memristors Using Electron Beam Lithography, *International Congress on Human-Computer Interaction, Optimization and Robotic Applications (HORA)*, 2020.
48 Q. Xia, *et al.*, Nanoimprint lithography enables memristor crossbars and hybrid circuits, *Appl. Phys. A*, 2015, **121**(2), 467–479.
49 M. Franco, *et al.*, Printed Memristors: An Overview of Ink, Materials, Deposition Techniques, and Applications, *Ad. Electron. Mater.*, 2024, **10**(10), 2400212.
50 C. Kapat, B. Pradhan and B. Bhattacharjee, Potentiostatic study of reinforcing steel in chloride contaminated concrete powder solution extracts, *Corros. Sci.*, 2006, **48**(7), 1757–1769.
51 B. Pradhan and B. Bhattacharjee, Corrosion zones of rebar in chloride contaminated concrete through potentiostatic study in concrete powder solution extracts, *Corros. Sci.*, 2007, **49**(10), 3935–3952.
52 S. P. Adhikari, *et al.*, Three Fingerprints of Memristor, in *Handbook of Memristor Networks*, ed. L. Chua, G. C. Sirakoulis and A. Adamatzky, Springer International Publishing, Cham, 2019, pp. 165–196.
53 L. Chua, If it's pinched it'sa memristor, *Semicond. Sci. Technol.*, 2014, **29**(10), 104001.
54 S. Dai, *et al.*, Recent Advances in Transistor-Based Artificial Synapses, *Adv. Funct. Mater.*, 2019, **29**(42), 1903700.
55 J. J. Maraj, *et al.*, Short-Term Facilitation-Then-Depression Enables Adaptive Processing of Sensory Inputs by Ion Channels in Biomolecular Synapses, *ACS Appl. Electron. Mater.*, 2021, **3**(10), 4448–4458.
56 R. S. Zucker and W. G. Regehr, Short-term synaptic plasticity, *Annu. Rev. Physiol.*, 2002, **64**(1), 355–405.
57 C. F. Stevens and J. F. Wesseling, Augmentation is a potentiation of the exocytotic process, *Neuron*, 1999, **22**(1), 139–146.
58 V. S. Dongle, *et al.*, Development of self-rectifying ZnO thin film resistive switching memory device using successive ionic layer adsorption and reaction method, *J. Mater. Sci.: Mater. Electron.*, 2018, **29**(21), 18733–18741.
59 V. S. Markin, A. G. Volkov and L. Chua, An analytical model of memristors in plants, *Plant Signaling Behav.*, 2014, **9**(10), e972887.
60 O. Pabst and Ø. G. Martinsen, Simulation based comparison between a transversal and a tangential memristor model with a capacitance in parallel, *PLoS One*, 2019, **14**(8), e0221533.
61 D. Kim, *et al.*, Understanding the Electrical Characteristics of Electrochemical Metallization Memristors through Identification of Conduction Channel in Entire Active Area, *Electron. Mater. Lett.*, 2024, **20**(5), 525–536.
62 T. Tsuruoka, *et al.*, Redox reactions at Cu, Ag/Ta_2O_5 interfaces and the effects of Ta_2O_5 film density on the forming process in atomic switch structures, *Adv. Funct. Mater.*, 2015, **25**(40), 6374–6381.
63 L. Jamilpanah and S. M. Mohseni, Facilitate Measurement of Electrochemical Reactions in Redox-Based Memristors by Simply Thickening the Electrolyte Layer, *Phys. Status Solidi RRL*, 2018, **12**(5), 1800046.
64 A. Bard, *Standard potentials in aqueous solution*, Routledge, 2017.
65 S. G. Naik and M. H. K. Rabinal, Significance of electrode contact area on memristive parameters of silver iodide, *Mater. Sci. Semicond. Process.*, 2022, **138**, 106309.

 This journal is © The Royal Society of Chemistry 2025

Open Access Article. Published on 13 May 2025. Downloaded on 3/6/2026 3:41:36 AM. This article is licensed under a Creative Commons Attribution 3.0 Unported Licence.

66 W. Chen, *et al.*, Essential Characteristics of Memristors for Neuromorphic Computing, *Adv. Electron. Mater.*, 2023, **9**(2), 2200833.
67 E. Gale, B. de Lacy Costello and A. Adamatzky, The effect of electrode size on memristor properties: an experimental and theoretical study, in 2012 IEEE International Conference on Electronics Design, Systems and Applications (ICEDSA), IEEE, 2012.
68 M. Ismail, *et al.*, Demonstration of synaptic and resistive switching characteristics in W/TiO_2/HfO_2/TaN memristor crossbar array for bioinspired neuromorphic computing, *J. Mater. Sci. Technol.*, 2022, **96**, 94–102.
69 M. Lanza, *et al.*, Standards for the Characterization of Endurance in Resistive Switching Devices, *ACS Nano*, 2021, **15**(11), 17214–17231.
70 M. J. Caire, V. Reddy and M. Varacallo, *Physiology, Synapse*, StatPearls Publishing, Treasure Island (FL), 2023.
71 A. Citri and R. C. Malenka, Synaptic Plasticity: Multiple Forms, Functions, and Mechanisms, *Neuropsychopharmacology*, 2008, **33**(1), 18–41.
72 Y. van de Burgt, *et al.*, A non-volatile organic electrochemical device as a low-voltage artificial synapse for neuromorphic computing, *Nat. Mater.*, 2017, **16**(4), 414–418.
73 K. Kang, *et al.*, High-Performance Solution-Processed Organo-Metal Halide Perovskite Unipolar Resistive Memory Devices in a Cross-Bar Array Structure, *Adv. Mater.*, 2019, **31**(21), 1804841.
74 X. Yan, *et al.*, Vacancy-Induced Synaptic Behavior in 2D WS2 Nanosheet–Based Memristor for Low-Power Neuromorphic Computing, *Small*, 2019, **15**(24), 1901423.
75 B. Zhao, *et al.*, Reproducible and low-power multistate biomemristor from interpenetrating network electrolyte design, *InfoMat*, 2022, **4**(11), e12350.
76 E. J. Yoo, *et al.*, Resistive Switching Behavior in Organic-Inorganic Hybrid CH3 NH3 PbI3-x Clx Perovskite for Resistive Random Access Memory Devices, *Adv. Mater.*, 2015, **27**(40), 6170–6175.
77 X. Liu, *et al.*, Flexible Transparent High-Efficiency Photoelectric Perovskite Resistive Switching Memory, *Adv. Funct. Mater.*, 2022, **32**(38), 2202951.
78 X. Feng, *et al.*, A novel nonvolatile memory device based on oxidized $Ti_3C_2T_x$ MXene for neurocomputing application, *Carbon*, 2023, **205**, 365–372.
79 Y. Wang, *et al.*, MXene-ZnO Memristor for Multimodal In-Sensor Computing, *Adv. Funct. Mater.*, 2021, **31**(21), 2100144.
80 R. Tahir, *et al.*, Multiferroic and ferroelectric phases revealed in 2D $Ti_3C_2T_x$ MXene film for high performance resistive data storage devices, *npj 2D Mater. Appl.*, 2023, **7**(1), 7.
81 C. Zhang, *et al.*, Visual growth of nano-HOFs for low-power memristive spiking neuromorphic system, *Nano Energy*, 2023, **109**, 108274.
82 T. V. P. Bliss and S. F. Cooke, Long-term potentiation and long-term depression: a clinical perspective, *Clinics*, 2011, **66**, 3–17.
83 S. Yu, *et al.*, An Electronic Synapse Device Based on Metal Oxide Resistive Switching Memory for Neuromorphic Computation, *IEEE Trans. Electron Devices*, 2011, **58**(8), 2729–2737.
84 S. H. Jo, *et al.*, Nanoscale Memristor Device as Synapse in Neuromorphic Systems, *Nano Lett.*, 2010, **10**(4), 1297–1301.
85 B.-Y. Kim, *et al.*, Nanogenerator-induced synaptic plasticity and metaplasticity of bio-realistic artificial synapses. NPG Asia, *Materials*, 2017, **9**(5), e381–e381.
86 T.-H. Lee, *et al.*, Synaptic Plasticity and Metaplasticity of Biological Synapse Realized in a $KNbO_3$ Memristor for Application to Artificial Synapse, *ACS Appl. Mater. Interfaces*, 2018, **10**(30), 25673–25682.
87 J. S. Najem, *et al.*, Memristive Ion Channel-Doped Biomembranes as Synaptic Mimics, *ACS Nano*, 2018, **12**(5), 4702–4711.
88 X. Yao, *et al.*, Protonic solid-state electrochemical synapse for physical neural networks, *Nat. Commun.*, 2020, **11**(1), 3134.
89 A. J. Smith, S. Owens and I. D. Forsythe, Characterisation of inhibitory and excitatory postsynaptic currents of the rat medial superior olive, *J. Physiol.*, 2000, **529**(3), 681–698.
90 S. Brenowitz, J. David and L. Trussell, Enhancement of Synaptic Efficacy by Presynaptic GABAB Receptors, *Neuron*, 1998, **20**(1), 135–141.
91 C. Xu, *et al.*, GABAB receptor activation mediates frequency-dependent plasticity of developing GABAergic synapses, *Nat. Neurosci.*, 2008, **11**(12), 1410–1418.
92 W. Xiong, *et al.*, Bilayered Oxide-Based Cognitive Memristor with Brain-Inspired Learning Activities, *Adv. Electron. Mater.*, 2019, **5**(8), 1900439.
93 Y. She, *et al.*, Oxygen Vacancy-Dependent Synaptic Dynamic Behavior of TiOx-Based Transparent Memristor, *IEEE Trans. Electron Devices*, 2021, **68**(4), 1950–1955.
94 W. Huh, *et al.*, Synaptic Barristor Based on Phase-Engineered 2D Heterostructures, *Adv. Mater.*, 2018, **30**(35), 1801447.
95 K. He, *et al.*, Artificial Neural Pathway Based on a Memristor Synapse for Optically Mediated Motion Learning, *ACS Nano*, 2022, **16**(6), 9691–9700.
96 A. Kirkwood, M. G. Rioult and M. F. Bear, Experience-dependent modification of synaptic plasticity in visual cortex, *Nature*, 1996, **381**(6582), 526–528.
97 C. Zhang, *et al.*, Bioinspired Artificial Sensory Nerve Based on Nafion Memristor, *Adv. Funct. Mater.*, 2019, **29**(20), 1808783.
98 J. Li, *et al.*, Polymeric Memristor Based Artificial Synapses with Ultra-Wide Operating Temperature, *Adv. Mater.*, 2023, **35**(23), 2209728.
99 L. Hu, *et al.*, Ultrasensitive Memristive Synapses Based on Lightly Oxidized Sulfide Films, *Adv. Mater.*, 2017, **29**(24), 1606927.
100 T. Chang, S.-H. Jo and W. Lu, Short-Term Memory to Long-Term Memory Transition in a Nanoscale Memristor, *ACS Nano*, 2011, **5**(9), 7669–7676.
101 S. Deswal, A. Kumar and A. Kumar, NbOx based memristor as artificial synapse emulating short term plasticity, *AIP Adv.*, 2019, **9**(9), 095022.

Open Access Article. Published on 13 May 2025. Downloaded on 3/6/2026 3:41:36 AM.
This article is licensed under a Creative Commons Attribution 3.0 Unported Licence.

102 L. Q. Zhu, *et al.*, Artificial synapse network on inorganic proton conductor for neuromorphic systems, *Nat. Commun.*, 2014, **5**(1), 3158.
103 X. Yan, *et al.*, Memristor with Ag-cluster-doped TiO_2 films as artificial synapse for neuroinspired computing, *Adv. Funct. Mater.*, 2018, **28**(1), 1705320.
104 L. Zhou, *et al.*, Tunable synaptic behavior realized in C_3N composite based memristor, *Nano Energy*, 2019, **58**, 293–303.
105 W. B. Levy and O. Steward, Temporal contiguity requirements for long-term associative potentiation/depression in the hippocampus, *Neuroscience*, 1983, **8**(4), 791–797.
106 B. Gustafsson, *et al.*, Long-term potentiation in the hippocampus using depolarizing current pulses as the conditioning stimulus to single volley synaptic potentials, *J. Neurosci.*, 1987, **7**(3), 774.
107 D. Debanne, B. H. Gähwiler and S. M. Thompson, Asynchronous pre- and postsynaptic activity induces associative long-term depression in area CA1 of the rat hippocampus in vitro, *Proc. Natl. Acad. Sci. U. S. A.*, 1994, **91**(3), 1148–1152.
108 N. Caporale and Y. Dan, Spike Timing–Dependent Plasticity: A Hebbian Learning Rule, *Annu. Rev. Neurosci.*, 2008, **31**, 25–46.
109 D. O. Hebb, *The organization of behavior: A neuropsychological theory*, Psychology Press, 2002.
110 M. C. W. van Rossum, G. Q. Bi and G. G. Turrigiano, Stable Hebbian Learning from Spike Timing-Dependent Plasticity, *J. Neurosci.*, 2000, **20**(23), 8812.
111 M. Prezioso, *et al.*, Self-Adaptive Spike-Time-Dependent Plasticity of Metal-Oxide Memristors, *Sci. Rep.*, 2016, **6**(1), 21331.

 This journal is © The Royal Society of Chemistry 2025